SARS-CoV-2 Infects Peripheral and Central Neurons of Mice Before Viremia, Facilitated by Neuropilin-1

Jonathan D. Joyce[1,5], Greyson A. Moore[2], Poorna Goswami[1], Emma H. Leslie[1], Christopher K. Thompson[3], and Andrea S. Bertke[4,5*]

[1]Translational Biology, Medicine, and Health, Virginia Polytechnic Institute & State University, Blacksburg, VA, USA; jjoyce84@vt.edu, ehenry20@vt.edu, poorna08@vt.edu

[2]Biomedical and Veterinary Science, Virginia Maryland College of Veterinary Medicine, Virginia Polytechnic Institute & State University, Blacksburg, VA, USA; gamoore@vt.edu

[3]School of Neuroscience, Virginia Polytechnic Institute & State University, Blacksburg, VA, USA; ckt@vt.edu

[4]Population Health Sciences, Virginia Maryland College of Veterinary Medicine, Virginia Polytechnic Institute & State University, Blacksburg, VA, USA; asbertke@vt.edu

[5]Center for Emerging Zoonotic and Arthropod-borne Pathogens, Virginia Polytechnic Institute & State University, Blacksburg, VA, USA

* Correspondence: asbertke@vt.edu

Abstract

Neurological symptoms are increasingly associated with COVID-19, suggesting that SARS-CoV-2 is neuroinvasive. Although studies have focused on neuroinvasion through infection of olfactory neurons and supporting cells or hematogenous spread, little attention has been paid to the susceptibility of the peripheral nervous system to infection or to alternative routes of neural invasion. We show that neurons in the central and peripheral nervous systems are susceptible to productive infection with SARS-CoV-2. Infection of K18-hACE2 mice, wild-type mice, and primary neuronal cultures demonstrates viral RNA, protein, and infectious virus in peripheral nervous system neurons, spinal cord, specific brain regions, and satellite glial cells. Moreover, we found that SARS-CoV-2 infects neurons at least in part via neuropilin-1. Our data show that SARS-CoV-2 rapidly invades and establishes productive infection in previously unassessed sites in the nervous system via direct invasion of neurons before viremia, which may underlie some cognitive and sensory symptoms associated with COVID-19.

Introduction

Up to 80% of people infected with SARS-CoV-2, the virus responsible for coronavirus disease 2019 (COVID-19), report neurological symptoms. These symptoms span the central nervous system (CNS; dizziness, headache, cognitive and memory deficits) and peripheral nervous system (PNS-somatic and autonomic systems; impaired taste, smell, sensation, orthostatic intolerance, syncope)[1-3]. Fatigue, memory issues, “brain fog,” and autonomic dysfunction can persist as part of post-acute sequalae of SARS-CoV-2 infection (“long COVID”)[4]. Detection of virus, viral RNA, and antigen, in cerebrospinal fluid (CSF) and brains of COVID-19 patients indicates SARS-CoV-2 is neuroinvasive, which has been documented for common-cold coronaviruses (HCoV-OC43, HCoV-229E) and epidemic coronaviruses (MERS, SARS)[5-13].

As anosmia is a primary symptom of COVID-19, studies were previously conducted to assess the possibility of CNS invasion via olfactory sensory neurons (OSNs), using transgenic mice expressing human angiotensin converting enzyme 2 (hACE2), the receptor for SARS-CoV-2[14-16]. Since RNA, protein, and virus were detected in OSNs, sustentacular cells, and brain homogenates, little attention has since been paid to alternative routes of neural invasion or to the role of PNS infection. Further, different regions of the brain have only recently come under scrutiny. Given that PNS symptoms are more commonly reported than CNS symptoms among non-hospitalized COVID-19 patients, who constitute the bulk of those infected, study of the susceptibility of the PNS to infection is needed[17].

Therefore, we assessed the susceptibility of PNS sensory (dorsal root ganglia-DRG, trigeminal ganglia-TG) and autonomic (superior cervical ganglia-SCG) neurons to infection with SARS-CoV-2 following intranasal inoculation of K18-hACE2 transgenic mice (hACE2 mice), wild-type C57BL/6J mice (WT), and guinea pigs (GPs). We also assessed neuroinvasion of the spinal cord and specific brain regions (olfactory bulb, cortex, hippocampus, brainstem, cerebellum), characterized viral growth kinetics in primary neuronal cultures, and investigated the contribution of neuropilin-1 (NRP-1) to neuronal entry.

We show that PNS sensory neurons are susceptible and permissive to productive infection with SARS-CoV-2 but that autonomic neurons, while susceptible to infection, sustain significant cytopathology and do not release infectious virus. Recovery of infectious virus from the TG, which innervates oronasal mucosa and extends central projections into the brainstem, suggests an alternative route of neuroinvasion independent of OSNs. We also show that infectious virus can be recovered from spinal cord and lumbosacral DRGs, which may underlie some sensory disturbances experienced in COVID-19. We further show that SARS-CoV-2 is capable of replicating in specific brain regions, with highest RNA concentrations and viral titers found in the hippocampus, which may contribute to memory disturbances associated with COVID-19. Furthermore, invasion of the brain and PNS occurs rapidly after infection, before viremia, demonstrating direct entry and transport through neurons. Our detection of viral RNA and infectious virus in brains and peripheral ganglia of WT mice demonstrates that neuroinvasion can occur independent of hACE2 and is at least partially dependent on NRP-1. Additionally, we show that GPs are resistant to intranasal SARS-CoV-2 infection.

Results

To assess the susceptibility of PNS and CNS neurons to SARS-CoV-2 infection, we intranasally (IN) inoculated hACE2 mice, WT mice, and GPs with 10^3 PFU (n=12 each) or 10^5 PFU (hACE2 n=12-14 each) SARS-CoV-2 USA-WA1/2020 (Extended Data Fig. 1a). Animals were monitored daily and tissues collected three- and six-days post-infection (dpi). Weight loss began after 3 dpi and death occurred at 6 dpi (14%) in hACE2 mice inoculated with 10^5 PFU. All other mice survived (Extended Data Fig. 1b). RT-qPCR showed low-level transient viremia with minimal invasion of the viscera (Extended Data Fig. 2), with highest viral RNA concentrations in lungs. These results are similar to previous studies and demonstrate our successful infection of these mice[16, 18, 19]. Infected GPs gained weight slower than uninfected controls and had mild increase in temperature without signs of disease (Extended Data Fig. 1b). Viral RNA was not detected in any tissues and no viral antigen was detected in lung or brains by immunostaining for SARS-CoV-2 nucleocapsid (SARS-N) (Extended Data Fig. 3).

PNS sensory TG and sympathetic SCG neurons innervating the oronasopharynx are susceptible to infection. Both sensory and sympathetic pathways through TGs and SCGs,

respectively, could serve as neural routes for neuroinvasion. The trigeminal nerve provides sensory innervation to the nasal septum, as well as oronasal mucosa, and projects into the brainstem. The SCG provides sympathetic innervation to salivary glands and vasculature of the head and brain, with preganglionic neurons residing in the spinal cord. To assess susceptibility of these peripheral neurons to infection with SARS-CoV-2, TGs and SCGs were assessed for viral RNA, protein, and infectious virus. We detected viral RNA at 3- and 6-dpi in TGs and SCGs in both inoculum groups in hACE2 and WT mice. Viral RNA concentrations were lower in WT than hACE2 mice (Fig. 1a-b). RNA concentrations increased over time in TGs and SCGs of hACE2 and WT mice, suggesting genome replication. Immunostaining detected SARS-N in the majority of TG neurons of hACE2 mice, as well as in ≈30% of TG neurons of WT mice (Fig. 1c, Extended Data Fig. 4). All SCG neurons from hACE2 mice were SARS-N-positive, showing substantial pathology with vacuolated neurons and loss of ganglionic architecture. Although SCGs from WT mice remained intact, SARS-N was evident in all neurons and some vacuolization was observed. Infectious virus was detected in TGs collected 3 dpi (0.5 log PFU/mg homogenate) and 6 dpi (2 log PFU/mg homogenate) from hACE2 mice. Infectious virus was not detected from SCGs. Considering the pathology of the ganglia, the virus may have produced such significant cytotoxicity that production of viral progeny was impossible. The use of multiple complementary assays indicate that viral RNA and protein can be isolated from both TGs and SCGs of both hACE2 and WT mice, and that infectious virus can be recovered from TGs. These data indicate that TGs and SCGs are susceptible to infection with SARS-CoV-2, that the TG may serve as a route of CNS invasion, and that neuroinvasion can occur independent of hACE2. All GPs were negative for viral RNA.

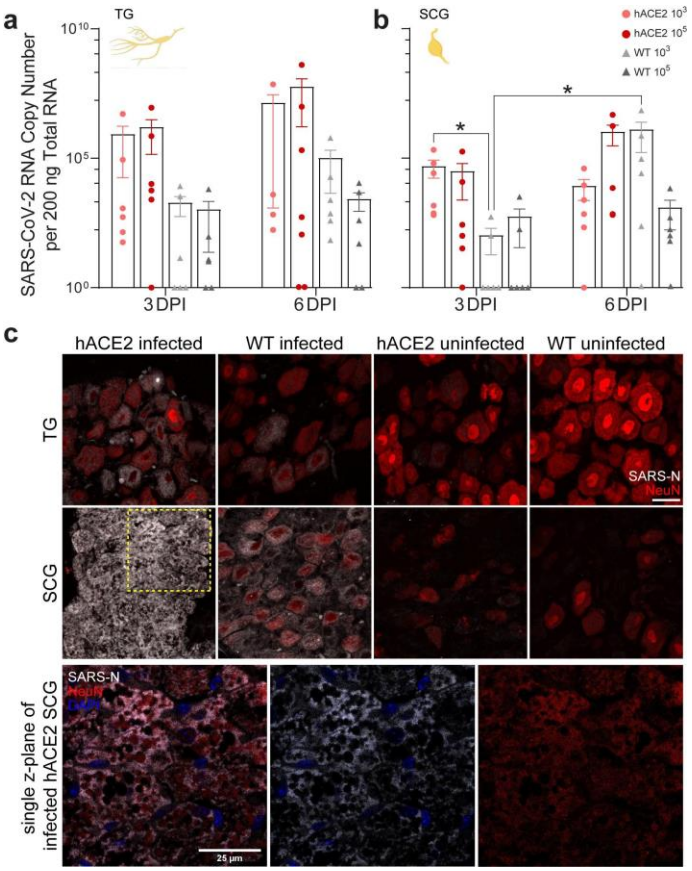

Fig 1. | SARS-CoV-2 infection of TG and SCG in hACE2 and wildtype (WT) mice. **a**, SARS-CoV-2 RNA was detected at increasing concentration in SCGs of hACE2 and WT mice in both inoculum groups from 3 to 6 DPI. The SCG provides sympathetic innervation to the salivary glands and blood vessels of the head, neck, and brain. Three-way ANOVA detected a significant difference ($F(7, 40) = 3.902$, $P = 0.0025$) in RNA genome copy number. Tukey's honestly significant difference (HSD) post hoc tests detected significant differences between the hACE2 and WT groups inoculated with 10^3 PFU assessed at 3 dpi ($p= 0.0464$) as well as the WT groups inoculated with 10^3 PFU assessed at 3- and 6-dpi ($p=0.029$). **b**, SARS-CoV-2 RNA was detected at increasing concentration in TGs of hACE2 and WT mice in both inoculum groups from 3 to 6 DPI. The TG provides sensory innervation to the face, including the nasal septum, and sends projections to the brain stem, thereby providing an alternative entry point for SARS-CoV-2. No statistically significant differences were detected between the groups ($F(7, 40) = 1.405$, $P = 0.2305$). **c**, Immunofluorescence for SARS-CoV-2 nucleocapsid (SARS-N, grey) and NeuN (red) labeled neurons in TG and SCG sections. SARS-N is more prevalent in hACE2 than in WT but observable in both. No SARS-N was detected in ganglia from uninfected animals. Neurons in SCG were particularly sensitive to infection; significant vacuolization was observed in infected hACE2 SCG cells, visible in single z-plane. Contrast for NeuN was increased in the z-plane to better illustrate residual NeuN immunoreactivity inside SARS-N-negative vacuoles in the highlighted box above. This cytopathology was common across numerous SCGs in both hACE2 and WT mice. Data are the mean ± s.e.m. Log transformed RNA genome copy numbers were statistically compared by three-way ANOVA (independent variables: inocula, days post infection, genotype). Pairwise comparisons were conducted using Tukey's HSD post hoc tests. *$p < 0.05$.

PNS sensory DRG and CNS spinal cord neurons are susceptible to infection. Extending our investigation beyond PNS innervations of the oronasopharynx to other peripheral ganglia, we assessed presence of SARS-CoV-2 RNA, protein, and infectious virus in the DRG. The DRG conveys sensory information (pain, pressure, position) from the periphery and internal organs to the spinal cord. Similar to our results from TGs, the sensory ganglia innervating the head, we detected viral RNA at 3- and 6-dpi in DRGs in both inoculum groups in hACE2 and WT mice (Fig. 2a). RNA concentrations increased over time, suggesting genome replication. Immunostaining demonstrated SARS-N in the majority of DRG neurons of hACE2 mice and a small percentage of WT mice (Fig. 2b, Extended Data Fig. 4). Furthermore, SARS-N immunostaining was observed in satellite glial cells in DRG neurons (Fig. 2c, Supplementary Video 1). Infectious SARS-CoV-2 was recovered from DRG homogenate of one hACE2 mouse (6 dpi), verifying productive infection (2 PFU/mg homogenate). Presence of viral RNA and infectious virus in neurons with no axonal targets in the head or lungs suggests spread via hematogenous dissemination or via axonal transport from a distal site of infection. Given that DRGs project to the spinal cord, and transmission from the DRG to the cord (or vice versa) is possible, the spinal cord was also assessed. We detected viral RNA at 3- and 6-dpi in both inoculum groups in hACE2 and WT mice (Fig. 2d). We identified punctate SARS-N staining inside spinal cord neurons, as well as diffuse SARS-N signal throughout the spinal cord (Fig. 2e, Extended Data Fig. 5, Supplementary Video 2) suggestive of free virus, or at least N protein, in the cord. Infectious virus (4 log PFU/mg homogenate) was recovered from the spinal cord of one hACE2 mouse (6 dpi), demonstrating productive infection. These data further demonstrate that PNS sensory neurons are susceptible to infection with SARS-CoV-2, as are CNS neurons in the spinal cord. All GPs were negative for viral RNA.

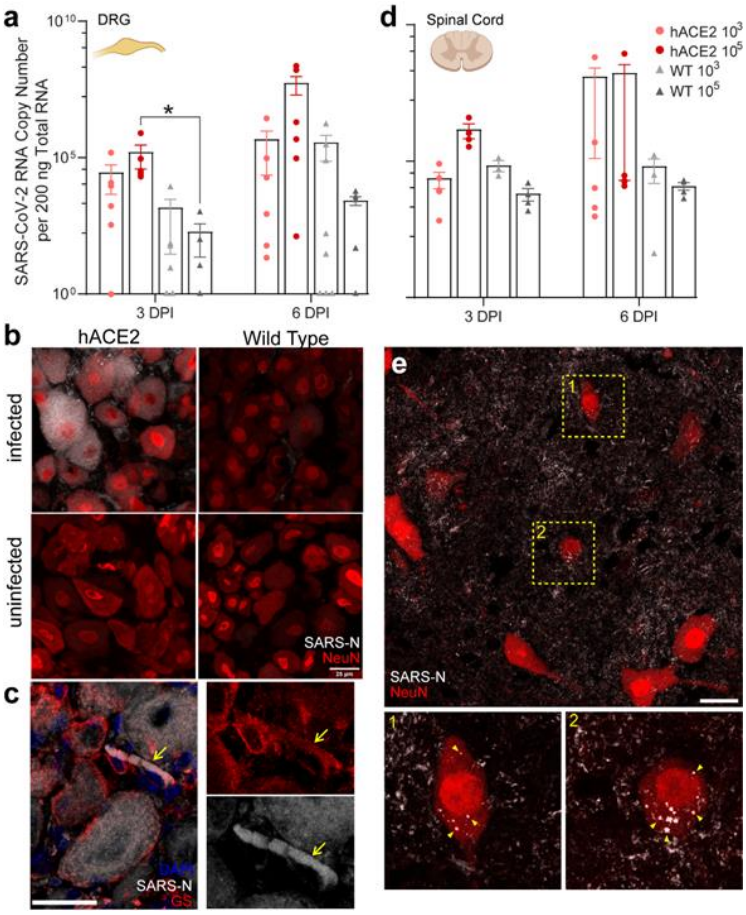

Fig 2. | SARS-CoV-2 infection of DRG, including satellite glial cells, and lumbosacral spinal cord in hACE2 and WT mice. a, SARS-CoV-2 RNA was detected in increasing concentrations in DRGs of hACE2 and WT mice in both inoculum groups from 3 to 6 DPI. The DRG conveys sensory information (pain, pressure, position) from the periphery and organs to the spinal cord. Three-way ANOVA detected a significant difference ($F(7, 41) = 4.163$, $P = 0.0015$) in RNA genome copy number. Tukey's HSD detected differences between the hACE2 and WT groups inoculated with 10^5 PFU at 3 dpi ($p = 0.022$). **b**, Immunofluorescence for SARS-N (grey) and NeuN (red) in DRG sections from infected and uninfected hACE2 and WT mice. SARS-N is more prevalent in hACE2 than in WT but observable in both. No SARS-N was detected in uninfected mice. Detection of RNA and SARS-N in peripheral neurons with no direct connection to the oronasopharynx suggests spread via hematogenous dissemination or via axonal transport. **c**, Immunofluorescence for SARS-N (grey) and glutamine synthetase (GS, red) in DRG sections from infected hACE2 mice. SARS-N was detected in numerous satellite glial cells (GS+) surrounding infected neurons, indicating neuronal support cells are also susceptible to infection. See Supplementary Video 1 for 3D rendering of this image. **d**, SARS-CoV-2 RNA was detected in lumbosacral spinal cords of hACE2 and WT mice in both inoculum groups at both time points. No statistically significant differences were detected between the groups ($F(7, 25) = 1.3054$, $P = 0.2885$). **e**, Representative image of immunofluorescence for SARS-N and NeuN in spinal cord cross-sections from an infected hACE2 mouse at 6 dpi. SARS-N was observed as discrete puncta (arrowheads in e1 and e2) in neuronal cytoplasm, reminiscent of viral replication complexes. See Supplementary Video 2 for 3D rendering of this image. Detection of RNA and SARS-N in the spinal cord demonstrates central neurons are susceptible to infection and may be infected directly from the DRG, brainstem, or hematogenously. Data are the mean ± s.e.m. Log-transformed RNA genome copy numbers were statistically compared by three-way ANOVA (independent variables: inocula, days post infection, genotype). Pairwise comparisons were conducted using Tukey's HSD post hoc tests. *$p < 0.05$.

Individual brain regions support varying levels of viral invasion and reproduction. While studies have assessed viral RNA and infectious virus in the brain, brain homogenates are typically tested, which doesn't allow for analysis of spatial differences in the presence of virus in discreet brain regions and could obscure detection of low levels of RNA or infectious virus in specific regions[14, 16, 20-22]. To determine if SARS-CoV-2 is present in specific brain regions, we assessed the olfactory bulb, hippocampus, cortex, brainstem, and cerebellum for SARS-CoV-2 RNA, protein, and infectious virus. We detected viral RNA in all brain regions at 3 dpi, which increased by 6 dpi (Fig. 3a-e), in both hACE2 and WT mice. Higher concentrations of viral RNA were found in hACE2 mice compared to WT mice in all regions. The highest RNA concentration was detected in the hippocampus at 6 dpi (Fig. 3b), followed by brainstem, cortex, olfactory bulb, and cerebellum in hACE2 mice. In WT mice, all regions contained similar quantities of SARS-CoV-2 RNA, suggesting that ACE2-independent spread or replication through the nervous system may differ compared to hACE2 mice. Infectious virus was recovered from the hippocampus and brainstem (3 log PFU/mg homogenate) and cortex as early as 3 dpi in hACE2 mice and from all regions by 6 dpi, with highest concentrations in the hippocampus and cortex (5 log PFU/mg homogenate) followed by olfactory bulb and brainstem (4 log PFU/mg homogenate) and cerebellum (2 log PFU/mg homogenate) (Fig. 3f). Unexpectedly, low levels of infectious virus were recovered from the hippocampi and brainstem of WT mice. These results indicate that viral invasion and replication is not consistent across the brain and the highest concentrations of virus are found in areas functionally connected to the olfactory and limbic systems, two systems strongly impacted during COVID-19. All GPs were negative for viral RNA.

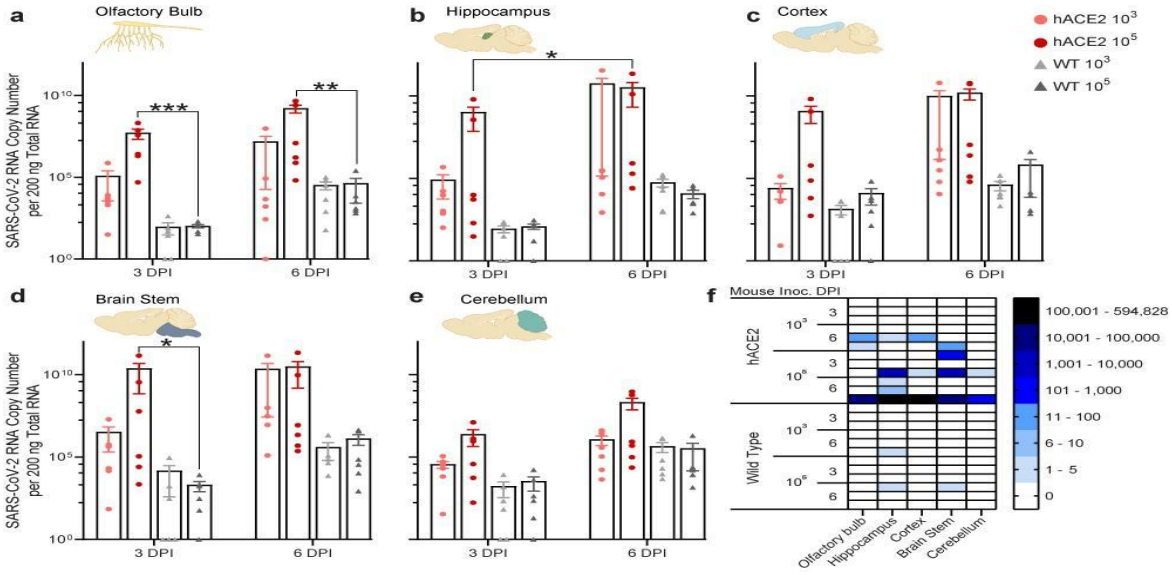

Fig 3. | SARS-CoV-2 infection of the olfactory bulb and various brain regions in hACE2 and WT mice. SARS-CoV-2 RNA was detected in increasing concentration in olfactory bulb **a**, hippocampus **b**, cortex **c**, brainstem **d**, and cerebellum **e**, of hACE2 and WT mice in both inoculum groups from 3 to 6 DPI. Three-way ANOVA detected a significant difference ($F(7, 41) = 12.556$, $P = 0.0001$) in RNA genome copy number in the olfactory bulb. Tukey's HSD detected differences in the olfactory bulb between hACE2 and WT groups inoculated with 10^5 PFU assessed at 3 dpi ($p<0.0001$) as well as between those groups assessed at 6 dpi ($p=0.001$). A significant difference ($F(7, 41) = 5.106$, $P = 0.0003$) was also detected in the hippocampi of hACE2 mice inoculated with 10^5 PFU assessed at 3- vs 6-dpi ($p=0.0017$). A significant

difference ($F(7, 41) = 6.917$, $P = <0.0001$) was also detected in the brainstem of the hACE2 and WT groups inoculated with 10^5 PFU assessed at 3 dpi ($p= 0.0103$). While differences were detected in the cortex ($F(7, 41) = 6.098$, $P = <0.0001$) and the cerebellum ($F(7, 41) = 6.652$, $P = <0.0001$) none were between relevant groups. **f**, Heatmap showing recovery of infectious SARS-CoV-2 from homogenates of the olfactory bulb and specific brain regions assessed for viral RNA. Recovery of infectious virus varied across individual animals with some having no regions with recoverable virus and some with virus in all regions. Of note, infectious virus was recovered from the hippocampi and brainstem of some WT mice, which are regions impacted in COVID-19 disease. Data are the mean ± s.e.m. Log transformed RNA genome copy numbers were statistically compared by three-way ANOVA (independent variables: inocula, days post infection, genotype). Pairwise comparisons were conducted using Tukey's HSD post hoc tests. *$p < 0.05$, **$p < 0.01$, ***$p < 0.001$.

To further assess localization of SARS-CoV-2 in brain regions, we immunostained sagittal sections of hACE2 brains for SARS-N and neuronal marker NeuN (Fig. 4, Extended Data Fig. 5). At 6 dpi, minimal SARS-N was found in the striatum, geniculate nucleus, superior colliculus, superior olive or cerebellum. In other regions, including frontal cortex, lateral preoptic area and visual cortex, thalamus and nucleus accumbens, the majority of neurons were positive. Some of these regions also showed diffuse SARS-N in tissue (cortex, reticular formation), suggesting differences in pathology within various brain regions. As the reticular formation facilitates motor activity associated with the vagus nerve, pathology in this region would correlate with vagus nerve dysfunction, which is associated with even mild COVID-19 cases[23]. Despite finding $>10^4$ copies of viral RNA in the olfactory bulb of all six hACE2 mice, infectious virus was recovered from only one of three mice and SARS-N was absent in the caudal olfactory bulb in assessed mice. However, axons of neurons with cytoplasmic N protein in the olfactory tubercle stained positive for SARS-N, suggesting axonal spread from the olfactory bulb into the olfactory tubercle, where productive infection ensues.

In the hippocampus (Fig. 5), neurons with cytoplasmic and axonal SARS-N were evident in the majority of CA1 and CA3 neurons, which receive input from the olfactory system through the entorhinal cortex, supporting axonal spread to the hippocampus. In contrast, the dentate gyrus had few SARS-N positive neurons.

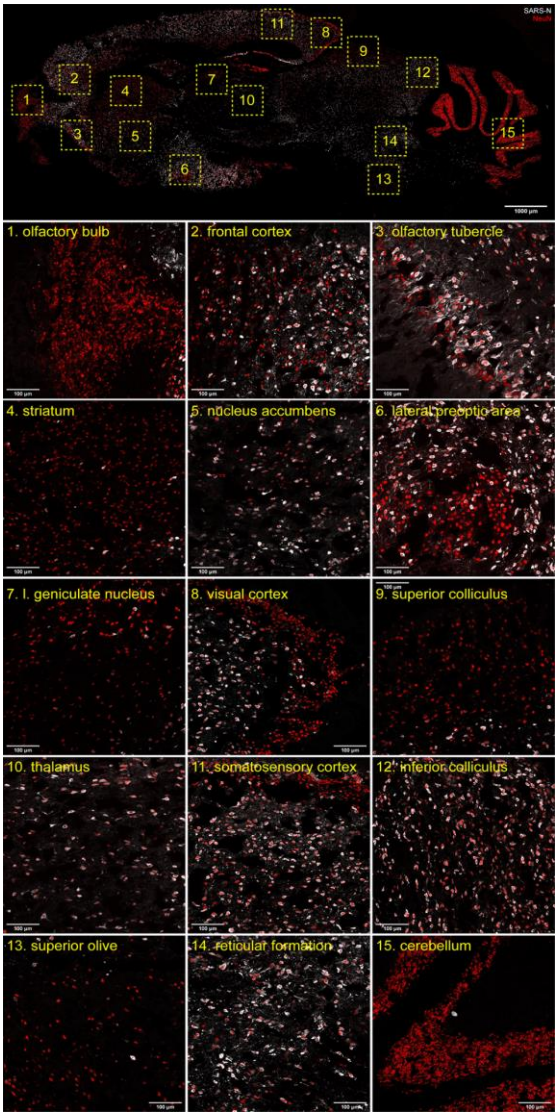

Fig 4. | Immunofluorescence for SARS-N (grey) and NeuN (red) in a parasagittal brain section from an infected hACE2 mouse assessed 6 DPI. SARS-N+ neurons were observed throughout multiple brain regions with some notable exceptions. Few SARS-N+ cells were detected in the granule cell layer of the olfactory bulb, the medium spiny neurons in the striatum, and the granule cells in the cerebellum. Relatively few SARS-N+ neurons were identified in the lateral geniculate nucleus, layers 2 and 3 of the visual cortex, and in the superior colliculus. This stood in contrast to adjacent non-visual areas (thalamus, somatosensory cortex, inferior colliculus), which had numerous SARS-N+ neurons. The fact that some of these areas contain GABAergic neurons suggests that inhibitory neurons may be spared infection, at least at this time point.

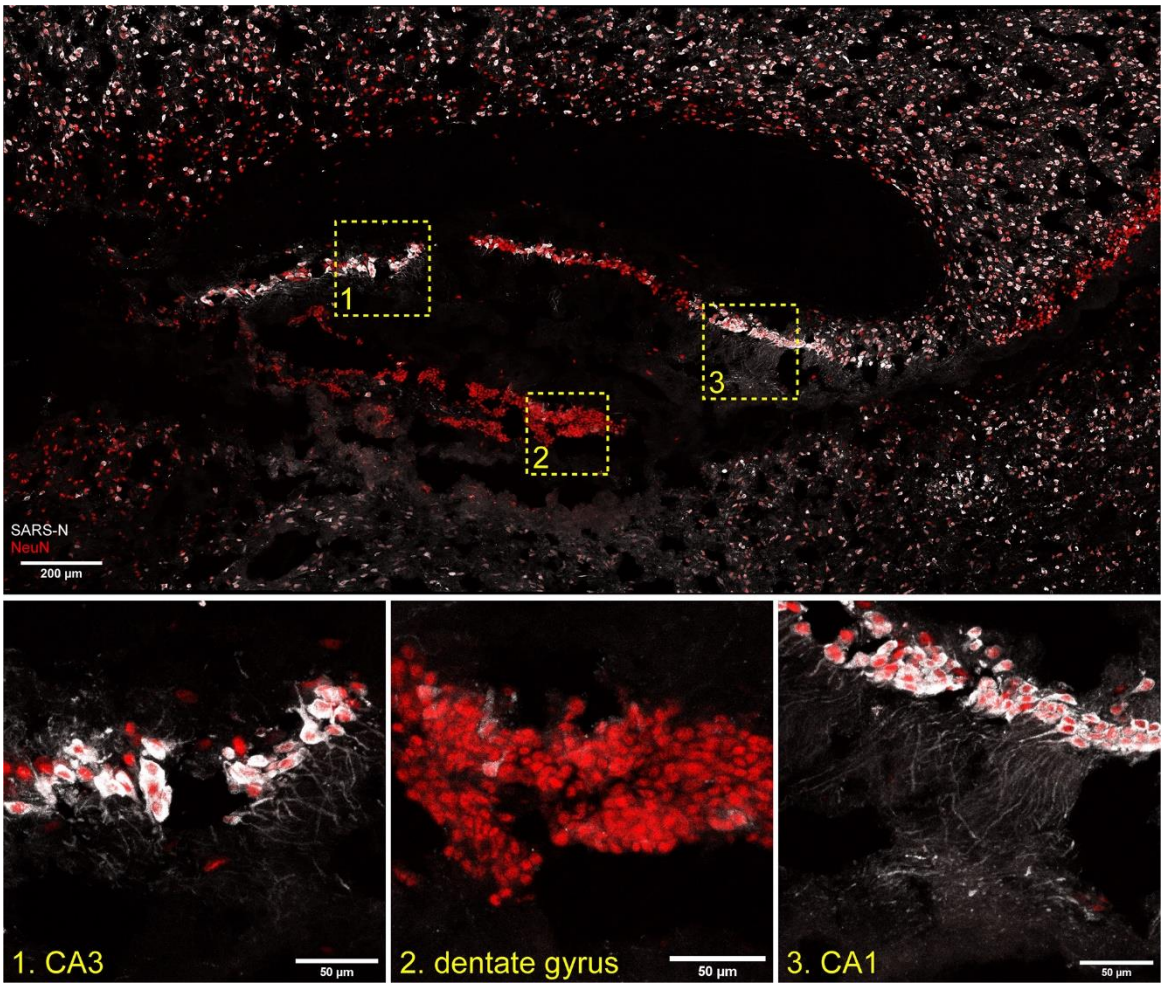

Fig 5. | Immunofluorescence for SARS-N (grey) and NeuN (red) in the hippocampus from an infected hACE2 mouse assessed 6 DPI. SARS-N+ neurons were observed in CA3 and CA1. Very few SARS-N+ neurons were detected in the granule cell layer of the dentate gyrus. Of note are SARS-N+ processes in infected neurons throughout the hippocampus, as seen in the magnified regions in lower panels.

SARS-CoV-2 productively infects primary cultured sensory but not autonomic neurons from adult mice. To confirm that PNS sensory and autonomic neurons are both susceptible and permissive to infection with SARS-CoV-2, resulting in release of infectious virus, and to establish basic replication kinetics of SARS-CoV-2 in neurons, DRGs, TGs, and SCGs were infected *ex-vivo*. Neurons were harvested from 8-10-week-old hACE2 and WT mice to establish primary neuronal cultures, which were then infected. Media and cells were analyzed separately for viral RNA (RT-qPCR) and infectious virus (plaque assay) to differentiate between intracellular replication and release of infectious virus. Viral RNA levels increased in SCG neurons between 2- and 3-dpi, although no increase in viral RNA was detected in media (Fig 6a). Infectious virus wasn't detected in the cellular or media fractions (Fig 6b). These data show that while viral genome replication occurs in SCGs, infectious virus is not released, suggesting abortive infection in sympathetic autonomic neurons. Considering the pathology of the SCGs *in vivo*, SARS-CoV-2 appears to be cytotoxic to SCG neurons prior to production of viral progeny. Viral RNA levels increased in TG neurons between 1- and 2-dpi, subsequently falling at 3 dpi (Fig 6a). Infectious virus was recovered from neurons and media from 2- to 4-dpi, declining at 5 dpi in both (Fig 6b),

indicating that in TG neurons, genome replication peaks at ~48 hpi, after which infectious virus is released. While DRGs follow a similar pattern, viral RNA levels exhibited a cyclical pattern with peaks occurring ~48 h intervals at 2- and 4-dpi (Fig 6a). Infectious virus was recovered from neurons and media in a similar fashion (Fig 6b). These data indicate successive rounds of genome amplification and infectious virus release occurs in DRGs, either within individual neurons without killing them or in additional neurons through a second infection cycle. Taken together, these data show that PNS sensory neurons are both susceptible and permissive to SARS-CoV-2 infection resulting in release of infectious virus. Also, they show that while autonomic neurons are susceptible to infection with SARS-CoV-2 and genome replication can occur, they are not permissive to release of infectious virus. In parallel, primary neuronal cultures were infected and fixed at 1, 2, and 3-dpi for immunostaining, which showed few DRG neurons (<5%,) in any culture became productively infected (Fig 6d), which is reflected in the modest increase in viral RNA and infectious virus (Fig 6a,b, Extended Data Fig. 6). In addition to genome replication, SCG neurons were permissive for N protein expression, shown by a positive immunofluorescence signal 1 dpi, while activated satellite glial cells accompanied dying neurons by 3 dpi (Fig 6c). In TG and DRG neurons, several phenotypes were observed, including perinuclear SARS-N staining at 1 dpi and punctate staining in the cytoplasm of enlarged neurons at 3 dpi, likely representing replication compartments (Fig 6c, Supplementary Video 3-4). Infected sensory neurons showed a variety of phenotypes, including loss of membrane integrity, cytoplasmic puncta, and seemingly healthy neurons strongly expressing SARS-N (Fig. 7 inset 1,2). Infected satellite glial cells, which appeared to be activated, were also present in some primary neuronal cultures (Fig. 7 inset 3).

Infection of WT neurons (Fig. 6a,b) showed viral RNA concentrations increased from 1-2 dpi in SCGs and increases in media at 2- and 4-dpi, similar to hACE2 neurons. Low levels of infectious virus were recovered in neurons and media at 1 dpi. In TGs, viral RNA concentrations cyclically peaked at 2- and 5-dpi with minimal increase in media, similar to hACE2 neurons. Low levels of infectious virus were recovered in neurons and media 1-2 dpi. Viral RNA concentrations in DRGs steadily increased from 1-4 dpi reaching similar levels to viral RNA concentrations in hACE2 DRGs at 4 dpi, with a concomitant increase in media. Low levels of infectious virus were recovered in media from 1-2 dpi but a second release, as from hACE2 neurons, was not apparent. These data show invasion and replication in neurons lacking hACE2, although reduced compared to hACE2-expressing neurons.

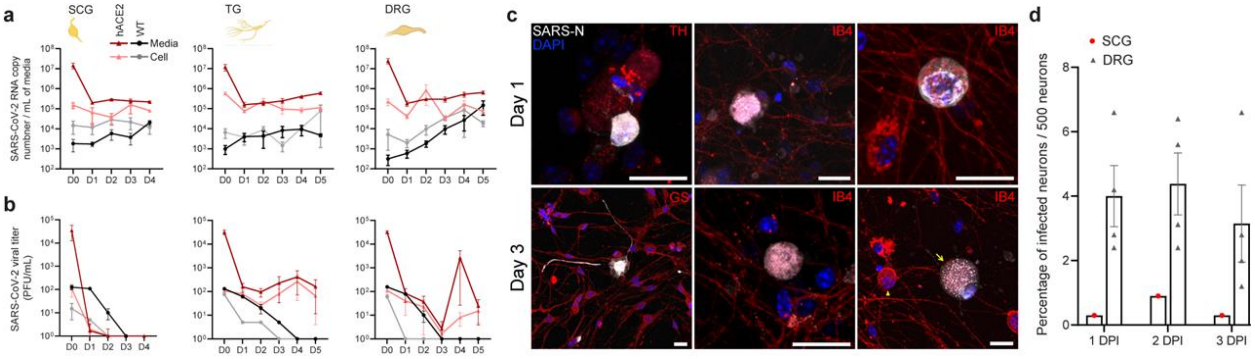

Fig 6. | SARS-CoV-2 infection of primary neuronal cultures from SCG, TG, DRG of hACE2 and WT mice. a, SARS-CoV-2 RNA was quantified by RT-qPCR separately in SCG, TG, and DRG neurons and media to generate a 4–5-day viral genome replication profile in neurons from hACE2 and WT mice. Viral

genome replication occurs in all neurons following similar patterns with differential infectious virus release into media. Intracellular replication patterns are similar between hACE2 and WT neurons, although at reduced levels in WT neurons. hACE2 DRGs have peaks in genome replication ~48 hpi and ~96 hpi indicating successive rounds of replication. **b**, Infectious virus was quantified by plaque assay on Vero E6 cells in SCG, TG, and DRG neuronal cultures to generate growth curves in primary neurons from hACE2 and WT mice. Infectious virus was not recovered from SCG neurons indicating abortive infection, likely mediated by cytotoxicity. Infectious virus was recovered from TG and DRG neurons indicating productive infection of these neurons. **c**, Immunofluorescence for SARS-N (grey) and either tyrosine hydroxylase (TH) or Isolectin-B4 (IB4) to counterstain neurons, or glutamine synthase (GS) to stain satellite glial cells. SARS-N was observed in neurons from each of the ganglia. Infected neurons were largely free of neurites by 1 dpi. At 3 dpi, many infected neurons exhibited cytopathologies such as degraded neurites, enlarged multi-nucleated cell bodies (arrow) compared to uninfected neurons (arrowhead), and SARS-N+ puncta reminiscent of viral replication compartments. See Supplementary Video 3 for 3D rendering of DRG at 3 dpi. See Supplementary Video 4 for 3D rendering of TG at 2 dpi. **d,** The percentage of hACE2 autonomic (SCG) and sensory (DRG) neurons positive for SARS-N were counted from 1-3 dpi. A small percentage of autonomic (SCG) neurons were visibly infected, with significant observable cell death, similar to *in vivo* observations. Infection in sensory (DRG) neurons were consistent from 1-3 dpi, with ~5% infected. Infection of *ex vivo* neurons is less efficient than *in vivo* infection. Scale bar = 20 μm. Data are the mean ± s.e.m

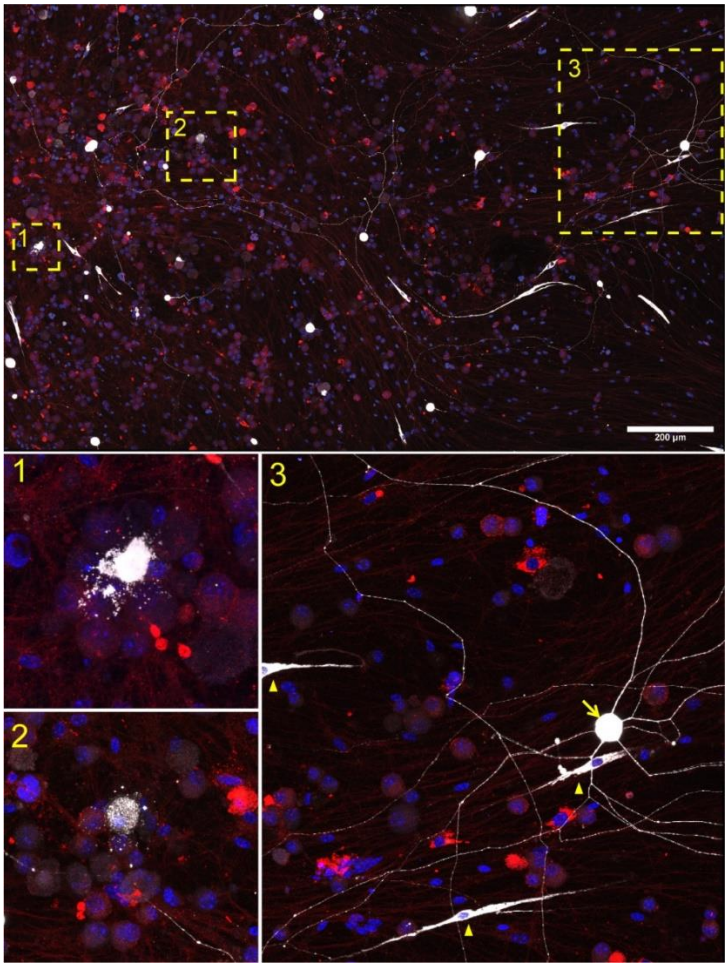

Fig 7. | SARS-CoV-2 infection of primary DRG neuronal cultures 3 DPI. Immunofluorescence for SARS-N (grey) and Isolectin-B4 (IB4) to counterstain neurons shows a variety of phenotypes of infected cells, including neurons with a loss of membrane integrity (1), SARS-N+ puncta within and surrounding neurons

(2), and seemingly healthy neurons with extensive neurites with strong SARS-N+ staining (arrow in 3). Infected satellite glial cells were also observed (arrowheads in 3); many appeared to be activated, noted by the presence of extended cellular processes. These findings are similar to immunostaining of DRGs *in vivo*, which also contained numerous infected satellite glial cells.

Neuroinvasion of the PNS and CNS occurs before viremia and involves neuropilin-1. To determine if neuroinvasion is driven by hematogenous entry or direct neuronal entry, PNS and CNS tissues were assessed 18 hpi and 42 hpi after intranasal inoculation of hACE2 and WT mice (Fig. 8a,b). Although no viral RNA was detected in blood at 18 hpi, viral RNA was detected in all PNS and CNS tissues and salivary glands (innervated by the SCG), with the exception of spinal cord and cerebellum of WT mice. By 42 hpi, viral RNA was detected in blood in a single hACE2 mouse and had increased in all hACE2 PNS and CNS tissues except SCG. In WT mice, viral RNA was no longer detected in salivary glands, SCG, or DRG but had increased in brainstem and hippocampus. Immunostaining did not detect SARS-N in any tissues, indicating that the virus was transiting through PNS tissues when collected but had not yet begun replication, which occurs later during infection. These data demonstrate that neuroinvasion occurs rapidly after infection, is mediated by invasion of and transport along neurons, and can occur independent of hACE2.

Since our WT mice were infected despite absence of hACE2, we investigated the contribution of neuropilin-1 (NRP-1) to neuronal entry in sensory neurons. NRP-1 has been shown to interact with SARS-CoV-2 spike, thereby enhancing viral binding and entry in non-neuronal cells[24-26]. Presence of NRP-1 was confirmed on DRG neurons and satellite glial cells via immunostaining (Fig. 8c). Primary cultured DRG neurons from hACE2 and WT mice were pretreated with EG00229, a selective NRP-1 antagonist, infected with SARS-CoV-2, and viral RNA concentrations were assessed 2 dpi. Viral RNA concentrations were significantly reduced by 99.8% in hACE2 neurons (p=0.0081) and 86.7% in WT neurons (p=0. 0141) (Fig. 8d), indicating that NRP-1 is a SARS-CoV-2 co-receptor in neurons irrespective of hACE2 expression.

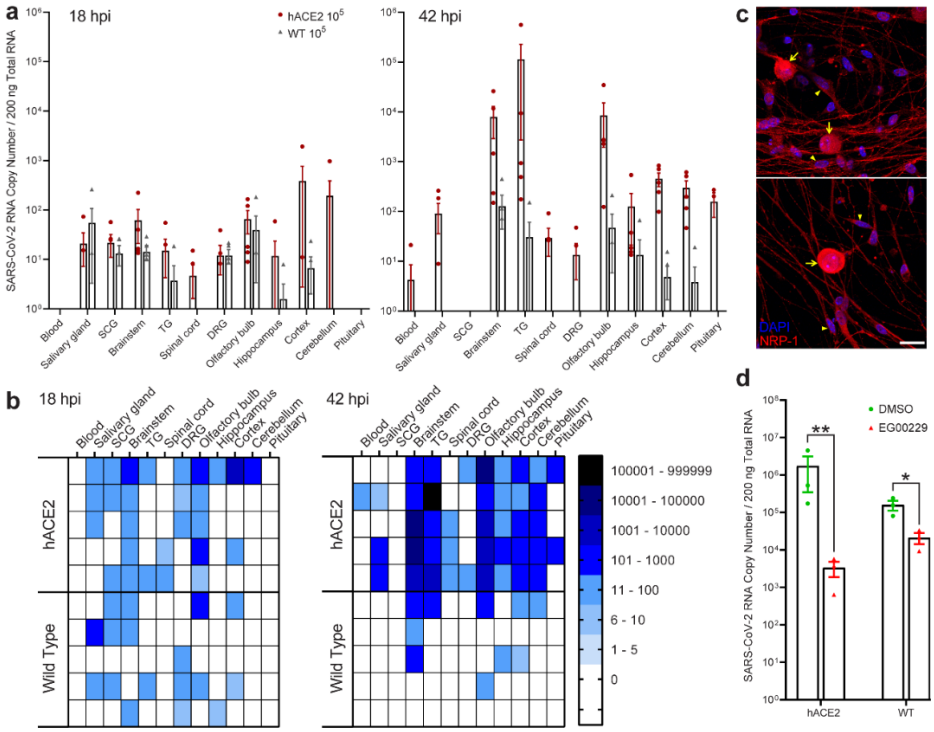

Fig 8. | Pre-viremic neuroinvasion of SARS-CoV-2 into PNS and CNS and the role of NRP-1 during neuronal entry. a, Although no viral RNA was detected in blood, low levels of SARS-CoV-2 RNA were detected in PNS and CNS of both hACE2 and WT mice as early as 18 hpi. CNS invasion in hACE2 and WT mice was common in olfactory bulb, hippocampus, cortex, and brainstem. Viral RNA was detected in PNS ganglia and the tissues they innervate (SCG-salivary gland, TG-brainstem) in both hACE2 and WT mice. Viral RNA was detected separately in the DRGs and spinal cords of some mice. By 42 hpi, viral RNA was detected in only one hACE2 mouse, but had increased in brainstem, TG and olfactory bulb, indicating replication in these tissues. **b**, Heatmaps visually displaying RT-qPCR values from panel a. Neuroinvasion in both PNS and CNS occurs rapidly before detectable viremia, thereby indicating direct neural entry and trans-synaptic spread of SARSs-CoV-2. Detection of viral RNA in the DRGs but not the spinal cord in some mice and vice versa in others indicates separate entry routes exist for the DRG and spinal cord. Invasion of the cord likely occurs from the brainstem, as all mice with early spinal cord infection also had brainstem infection. Invasion of the DRG may occur from the periphery. **c**, The transmembrane glycoprotein neuropilin-1 (NRP-1, red), shown to increase SARS-CoV-2 entry into non-neuronal cells, is expressed in neurons and satellite glial cells and was visualized by immunostaining. **d**, Treatment of hACE2 and WT DRG neurons with the NRP-1 antagonist EG00229 prior to infection with SARS-CoV-2 significantly reduced viral RNA concentrations at 2 dpi, the initial peak of viral replication in hACE2 DRG neurons, by 99.8% (p=0.0081) in hACE2 neurons and 86.7% (p=0. 0141) in WT neurons. Thus, NRP-1 is a critical co-receptor mediating viral entry into neurons expressing hACE2 and also enhances viral entry into WT neurons. These data also indicate that that additional host proteins are involved in neuronal entry. Scale bar = 20 μm. Data are the mean ± s.e.m.

Discussion

Neurotropic viruses can enter the nervous system hematogenously or through neural pathways. From blood, viruses can infect endothelial cells, gaining access to underlying tissues through lytic destruction of vasculature, or can be transported across the vasculature inside extravasating leukocytes. Viruses can enter neural pathways through peripheral sensory, autonomic, and/or motor axon terminals and transport retrograde toward the CNS, often moving trans-synaptically along functionally connected pathways. SARS-CoV-2 likely uses both mechanisms. SARS-CoV-2 CNS invasion has been proposed via infection of the nasal neuroepithelium with invasion of OSNs, the olfactory bulb, and its cortical projections[14-16, 18, 20-22]. Organoid, stem cell, microfluidic, and mouse models, correlating with human autopsy findings, demonstrate disruption of endothelial barriers and choroid plexus integrity, as well as transcytosis of SARS-CoV-2, supporting hematogenous CNS entry[5, 18, 27-31]. While OSNs are a key constituent of the nasal neuroepithelium, the oronasopharynx is innervated by other sensory and autonomic pathways through which SARS-CoV-2 may enter the nervous system. Utilizing hACE2 mice, WT mice, and primary neuronal cultures, we show susceptibility of peripheral neurons to SARS-CoV-2 infection, demonstrating differential replication kinetics and cytopathic outcomes following infection of sensory, autonomic, and central neurons. We also show evidence supporting axonal transport of SARS-CoV-2 and CNS entry, preceding viremia, through neural pathways that functionally connect to brain regions responsible for memory and cognition, which are affected in COVID-19. Furthermore, we show that SARS-CoV-2 can use NRP-1 for neuronal entry in the absence of hACE2 expression. As COVID-19 neurological symptoms are often related to peripheral neuron dysfunction rather than exclusive to CNS symptoms, focusing solely on CNS neuroinvasion takes a myopic view of the potential impacts of SARS-CoV-2 in the PNS.

Our detection of SARS-CoV-2 in the TG and SCG makes anatomical sense given their innervation of the oronasal mucosa and glands. Viral RNA concentrations were similar in the TG, SCG and olfactory bulb 18 hpi, indicating sensory and autonomic pathways are as susceptible to invasion

as the olfactory system. Although few autopsy studies have included the TG, our results complement findings of viral RNA, axonal damage, and neuron loss in the TGs of COVID-19 patients[31, 32]. While viral RNA and protein have been detected in salivary glands of COVID-19 patients, and infectious virus has been recovered from saliva, no assessments have been made of the SCG in human autopsies[33-36]. Within the oronasopharynx, the SCG provides sympathetic nervous system innervation to the oronasal mucosa, salivary glands, and vasculature and would be a logical point for neuroinvasion. Our combined use of *in vivo* and *ex vivo* infections demonstrates that sensory trigeminal neurons are both susceptible and permissive to productive infection with SARS-CoV-2, culminating in release of infectious virus. Isolation of infectious virus from the TG has yet to be reported and further supports the hypothesis that the TG can serve as an alternative route for CNS invasion. Increasing reports of acute necrotizing hemorrhagic encephalopathy (AHNE) associated with COVID-19, often involving the medial temporal lobe, suggest that neuroinvasion may follow a similar pathway as other neurotropic viruses (HSV-1), which causes a nearly identical complication when it reaches the CNS from the TG. Invasion of the brainstem along projections of the TG could damage nuclei important in cardiorespiratory regulation, a feature of severe COVID-19, and at least one imaging study of a COVID-19 patient with AHNE suggested invasion of the brainstem via the TG[7]. The SCG may be of less concern for direct CNS invasion as our neuronal culture infection data indicate abortive infection. However, the pathology of the SCG following infection *in vivo* suggests that SARS-CoV-2 causes substantial, and perhaps irreparable, damage to sympathetic neurons. Although we did not examine thoracic ganglia or the sympathetic trunk, the cytopathology in the SCG has broader implications for cardiac function, which relies on autonomic regulation. It is notable that comparable viral RNA concentrations were detected in TGs and SCGs of WT mice, indicating that both tissues are equally susceptible to infection in the absence of hACE2.

While entry into the TG and SCG following intranasal inoculation was not unexpected, detection of SARS-CoV-2 in the DRG was. We detected viral RNA in the DRG at levels comparable to the TG, demonstrating that sensory neurons, despite their location, are equally susceptible to infection. How the virus reached such distal peripheral ganglia is uncertain. Given that viral RNA was detected in DRGs 18 hpi, preceding viremia, hematogenous spread is unlikely. Alternatively, retrograde axonal transport into the neuronal cell bodies within the ganglion could occur through central spinal cord projections or from peripheral targets. It is noteworthy that none of the mice with viral RNA in the DRG 18 hpi had RNA in the spinal cord and none with viral RNA in the cord had RNA in the DRG. However, virus was detected in both DRG and spinal cord by 3 dpi. All mice with early spinal cord infection also had brainstem infection. Thus, entry into spinal cord appears to follow CNS invasion at the brainstem but infection of DRG neurons is possible from either central or peripheral axon terminals. Once in the DRG, results from our primary neuronal cultures indicate that viral replication and release of infectious virus occurs cyclically every 48 h. As the virus infected a small percentage of sensory neurons in culture, this pattern likely represents two distinct cycles of productive infection. *In vivo*, however, the majority of DRG neurons were positive for SARS-N, suggesting that infection of sensory neurons within the host is more efficient than *ex vivo* infection of cultured neurons. Although COVID-19 symptoms can include tingling, numbness and burning in fingers and toes, which are indicative of nociceptor damage or dysfunction, DRG neurons have yet to be assessed for their susceptibility to infection with SARS-CoV-2, either in animal models or in human autopsies. However, ACE2 is expressed by a subset of nociceptors in human DRGs, particularly in lumbosacral ganglia[37]. Similarly, no systematic analyses of spinal cords have been conducted, although spinal cord involvement is becoming increasingly associated with COVID-19. A recent review of disorders of the spinal cord in COVID-19 posited that direct invasion of the cord by SARS-CoV-2 could cause these pathologies[38]. Our results

indicate that neurons in the spinal cord and in the DRG are susceptible to SARS-CoV-2 infection and provide a rationale for a deeper investigation of the DRG as a site of productive viral infection in COVID-19, as well as the possibility and direction of axonal transport, since infection of the DRGs may contribute to some sensory disturbances suffered by COVID-19 patients.

Our detection of viral RNA and infectious virus in specific brain regions is more granular than what has been previously reported and shows the hippocampus, cortex, and brainstem are all rapidly invaded by SARS-CoV-2 through neural pathways before viremia. TG neurons, with axonal projections to both oronasal epithelium and brainstem, or SCG neurons, with synaptic connectivity to salivary glands and brainstem, could deliver virus directly to the CNS. Viral RNA and protein have been detected in the olfactory bulb, brainstem, cerebellum, and cortex of COVID-19 patients[6, 39, 40]. Our results indicate that viral penetration and replication within the brain is dependent on the region assessed, which suggests the presence of factors (cell types, synaptic connections, vascularization level) that favor invasion and replication in some regions over others. Our detection of infectious virus in the hippocampi and brainstems of both WT and hACE2 mice further underscore the importance of these structures in COVID-19 pathology. Interestingly, there were substantially fewer infected cells in some aspects of the nervous system, which might be due to the particular time point assessed or to the types of neurons present in these areas. Notably, SARS-CoV-2 was detected in CNS and PNS of both hACE2 and WT mice, indicating that hACE2 expression is not a requirement for neuronal infection. We demonstrate that NRP-1, which was shown previously to mediate entry into non-neuronal cells, also mediates entry into neurons. Our inhibition of NRP-1 in cultured DRG neurons from hACE2 mice reduced infection to a greater extent than in neurons from WT mice, indicating that NRP-1 can serve as a co-receptor to enhance infection in the presence of hACE2 expression or an alternative receptor independent of hACE2.

Since GPs were used as an animal model for SARS-CoV-1, we also assessed their potential as a model for SARS-CoV-2[41, 42]. Contrary to previous studies using intraperitoneal inoculation, we show that GPs are resistant to intranasal infection, having no detectable viral RNA in any tissues tested and no SARS-N in lungs or brains. A previous study showed that SARS-CoV-1 did not efficiently infect transfected cells expressing gpACE2[43] and recent *in silico* modeling of SARS-CoV-2 spike protein and gpACE2 binding showed altered kinetics, which was believed to limit infectability[44, 45]. Our results provide direct *in vivo* confirmation, resolving the question of the susceptibility of GPs to infection with SARS-CoV-2 following intranasal inoculation.

The extent of both acute and long-term neurological impacts of SARS-CoV-2 are only beginning to be realized. The existence of sensory and autonomic disorders, lasting months beyond initial infection, necessitates a better understanding of the impact of SARS-CoV-2 on the entirety of the nervous system, not just the brain. No studies have assessed the susceptibility of TG or SCG neurons to productive infection by SARS-CoV-2 or to investigate their role in viral invasion of the CNS. Additionally, no studies have determined if distal sensory ganglia such as the DRG can support infection, let alone provide an avenue of infection to the spine. Our work expands what is known about the neuroinvasive potential of SARS-CoV-2 by showing that PNS sensory and autonomic neurons, supporting satellite glial cells, and CNS neurons in the spinal cord are all susceptible to, and in most cases permissive to, productive infection with SARS-CoV-2 via direct neural invasion rather than hematogenous spread. Presence of infectious virus in these tissues shows that routes of neuroinvasion exist beyond OSNs and that invasion can occur independent of ACE2 using NRP-1 as a co-receptor. Our findings support the need to investigate these sites of neuroinvasion to a greater depth than currently exists.

Online content statement

Any methods, additional references, Nature Research reporting summaries, source data, extended data, supplementary information, acknowledgements, peer review information; details of author contributions and competing interests; and statements of data and code availability are available at ___.

Main Text References

1. Shouman, K., *et al.* Autonomic dysfunction following COVID-19 infection: an early experience. *Clin Auton Res* **31**, 385-394 (2021).
2. Chou, S.H., *et al.* Global Incidence of Neurological Manifestations Among Patients Hospitalized With COVID-19-A Report for the GCS-NeuroCOVID Consortium and the ENERGY Consortium. *JAMA Netw Open* **4**, e2112131 (2021).
3. Mao, L., *et al.* Neurologic Manifestations of Hospitalized Patients With Coronavirus Disease 2019 in Wuhan, China. *JAMA Neurol* **77**, 683-690 (2020).
4. Yang, A.C., *et al.* Dysregulation of brain and choroid plexus cell types in severe COVID-19. *Nature* **595**, 565-571 (2021).
5. Paniz-Mondolfi, A., *et al.* Central nervous system involvement by severe acute respiratory syndrome coronavirus-2 (SARS-CoV-2). *J Med Virol* **92**, 699-702 (2020).
6. Puelles, V.G., *et al.* Multiorgan and Renal Tropism of SARS-CoV-2. *N Engl J Med* **383**, 590-592 (2020).
7. Virhammar, J., *et al.* Acute necrotizing encephalopathy with SARS-CoV-2 RNA confirmed in cerebrospinal fluid. *Neurology* **95**, 445-449 (2020).
8. Xiang, P., *et al.* Case Report: Identification of SARS-CoV-2 in Cerebrospinal Fluid by Ultrahigh-Depth Sequencing in a Patient With Coronavirus Disease 2019 and Neurological Dysfunction. *Front Med (Lausanne)* **8**, 629828 (2021).
9. Bonavia, A., Arbour, N., Yong, V.W. & Talbot, P.J. Infection of primary cultures of human neural cells by human coronaviruses 229E and OC43. *J Virol* **71**, 800-806 (1997).
10. Arbour, N. & Talbot, P.J. Persistent infection of neural cell lines by human coronaviruses. *Adv Exp Med Biol* **440**, 575-581 (1998).
11. Arbour, N., Day, R., Newcombe, J. & Talbot, P.J. Neuroinvasion by human respiratory coronaviruses. *J Virol* **74**, 8913-8921 (2000).
12. Dube, M., *et al.* Axonal Transport Enables Neuron-to-Neuron Propagation of Human Coronavirus OC43. *J Virol* **92** (2018).
13. Cheng, Q., Yang, Y. & Gao, J. Infectivity of human coronavirus in the brain. *EBioMedicine* **56**, 102799 (2020).
14. Kumari, P., *et al.* Neuroinvasion and Encephalitis Following Intranasal Inoculation of SARS-CoV-2 in K18-hACE2 Mice. *Viruses* **13** (2021).
15. Golden, J.W., *et al.* Human angiotensin-converting enzyme 2 transgenic mice infected with SARS-CoV-2 develop severe and fatal respiratory disease. *JCI Insight* **5** (2020).
16. Zheng, J., *et al.* COVID-19 treatments and pathogenesis including anosmia in K18-hACE2 mice. *Nature* **589**, 603-607 (2021).
17. Ding, H., *et al.* Neurologic manifestations of nonhospitalized patients with COVID-19 in Wuhan, China. *MedComm (2020)* (2020).
18. Oladunni, F.S., *et al.* Lethality of SARS-CoV-2 infection in K18 human angiotensin-converting enzyme 2 transgenic mice. *Nat Commun* **11**, 6122 (2020).
19. Johnson, B.A., *et al.* Loss of furin cleavage site attenuates SARS-CoV-2 pathogenesis. *Nature* **591**, 293-299 (2021).
20. Winkler, E.S., *et al.* SARS-CoV-2 infection of human ACE2-transgenic mice causes severe lung inflammation and impaired function. *Nat Immunol* **21**, 1327-1335 (2020).

21. Rathnasinghe, R., *et al.* Comparison of transgenic and adenovirus hACE2 mouse models for SARS-CoV-2 infection. *Emerg Microbes Infect* **9**, 2433-2445 (2020).
22. Yinda, C.K., *et al.* K18-hACE2 mice develop respiratory disease resembling severe COVID-19. *PLoS Pathog* **17**, e1009195 (2021).
23. Moyano, A.J., Mejia Torres, S. & Espinosa, J. Vagus nerve neuropathy related to SARS COV-2 infection. *IDCases* **26**, e01242 (2021).
24. Daly, J.L., *et al.* Neuropilin-1 is a host factor for SARS-CoV-2 infection. *Science* **370**, 861-865 (2020).
25. Cantuti-Castelvetri, L., *et al.* Neuropilin-1 facilitates SARS-CoV-2 cell entry and infectivity. *Science* **370**, 856-860 (2020).
26. Moutal, A., *et al.* SARS-CoV-2 spike protein co-opts VEGF-A/neuropilin-1 receptor signaling to induce analgesia. *Pain* **162**, 243-252 (2021).
27. Pellegrini, L., *et al.* SARS-CoV-2 Infects the Brain Choroid Plexus and Disrupts the Blood-CSF Barrier in Human Brain Organoids. *Cell Stem Cell* **27**, 951-961 e955 (2020).
28. Jacob, F., *et al.* Human Pluripotent Stem Cell-Derived Neural Cells and Brain Organoids Reveal SARS-CoV-2 Neurotropism Predominates in Choroid Plexus Epithelium. *Cell Stem Cell* **27**, 937-950 e939 (2020).
29. Rhea, E.M., *et al.* The S1 protein of SARS-CoV-2 crosses the blood-brain barrier in mice. *Nat Neurosci* **24**, 368-378 (2021).
30. Buzhdygan, T.P., *et al.* The SARS-CoV-2 spike protein alters barrier function in 2D static and 3D microfluidic in-vitro models of the human blood-brain barrier. *Neurobiol Dis* **146**, 105131 (2020).
31. Meinhardt, J., *et al.* Olfactory transmucosal SARS-CoV-2 invasion as a port of central nervous system entry in individuals with COVID-19. *Nat Neurosci* **24**, 168-175 (2021).
32. von Weyhern, C.H., Kaufmann, I., Neff, F. & Kremer, M. Early evidence of pronounced brain involvement in fatal COVID-19 outcomes. *Lancet* **395**, e109 (2020).
33. Tutuncu, E.E., Ozgur, D. & Karamese, M. Saliva samples for detection of SARS-CoV-2 in mildly symptomatic and asymptomatic patients. *J Med Virol* **93**, 2932-2937 (2021).
34. Ota, K., *et al.* Detection of SARS-CoV-2 using qRT-PCR in saliva obtained from asymptomatic or mild COVID-19 patients, comparative analysis with matched nasopharyngeal samples. *PLoS One* **16**, e0252964 (2021).
35. Huang, N., *et al.* SARS-CoV-2 infection of the oral cavity and saliva. *Nat Med* **27**, 892-903 (2021).
36. Song, J., *et al.* Systematic analysis of ACE2 and TMPRSS2 expression in salivary glands reveals underlying transmission mechanism caused by SARS-CoV-2. *J Med Virol* **92**, 2556-2566 (2020).
37. Shiers, S., *et al.* ACE2 and SCARF expression in human dorsal root ganglion nociceptors: implications for SARS-CoV-2 virus neurological effects. *Pain* **161**, 2494-2501 (2020).
38. Garg, R.K., Paliwal, V.K. & Gupta, A. Spinal cord involvement in COVID-19: A review. *J Spinal Cord Med*, 1-15 (2021).
39. Bulfamante, G., *et al.* First ultrastructural autoptic findings of SARS -Cov-2 in olfactory pathways and brainstem. *Minerva Anestesiol* **86**, 678-679 (2020).
40. Song, E., *et al.* Neuroinvasion of SARS-CoV-2 in human and mouse brain. *J Exp Med* **218** (2021).
41. Chepurnov, A.A., Dadaeva, A.A., Malkova, E.M., Kolesnikov, S.I. & Sandakhchiev, L.S. Symptoms of infection caused by SARS coronavirus in laboratory mice and guinea pigs. *Dokl Biol Sci* **397**, 310-313 (2004).
42. Liang, L., *et al.* Pathology of guinea pigs experimentally infected with a novel reovirus and coronavirus isolated from SARS patients. *DNA Cell Biol* **24**, 485-490 (2005).

43. Li, K.K., *et al.* Characterisation of animal angiotensin-converting enzyme 2 receptors and use of pseudotyped virus to correlate receptor binding with susceptibility of SARS-CoV infection. *Hong Kong Med J* **18 Suppl 3**, 35-38 (2012).
44. Brooke, G.N. & Prischi, F. Structural and functional modelling of SARS-CoV-2 entry in animal models. *Sci Rep* **10**, 15917 (2020).
45. Conceicao, C., *et al.* The SARS-CoV-2 Spike protein has a broad tropism for mammalian ACE2 proteins. *PLoS Biol* **18**, e3001016 (2020).

Methods

Ethics statement. This study was approved by the Virginia Polytechnic Institute & State University Institutional Animal Care and Use Committee (Protocol # 20-228, approved 02/01/2021). This study was carried out according to the US Department of Agriculture's Animal Welfare Act and the Public Health Service's Policy on Humane Care and Use of Laboratory Animals.

Cells and virus. SARS-CoV-2 isolate USA-WA1/2020 (NR-52281; BEI) was passaged twice using Vero E6 cells (CRL-1586, ATCC) to produce viral stock for all infections. USA-WA1/2020 was recovered from an oropharyngeal swab taken from a 35-year-old male in Washington state in January 2020 who was diagnosed with COVID-19 after returning from visiting family in Wuhan, China. Viral stocks were titrated in duplicate using a standard plaque assay on Vero E6 cells with agarose overlay[46]. Vero E6 cells were maintained following standard cell culture protocols.

Mouse infections. Eight to ten-week-old male and female B6.Cg-Tg(K18-ACE2)2Prlmn/J mice (Stock # 034860; Jackson Laboratory; n=12, 2 groups of 6 mice), and their wild-type C57BL/6J counterparts (n=12, 2 groups of 6 mice) were inoculated intranasally with SARS-CoV-2 isolate USA-WA1/2020 (Extended Data Fig 1a). Inoculations were carried out under ketamine/xylazine anesthesia in the on campus ABSL-3 facility after a one-day acclimation period. Mice received 20 µL of either 10^3 PFU (2 groups per mouse type) or 10^5 PFU (2 groups per mouse type) of SARS-CoV-2 in 1X PBS. The inoculum was split between the nares for each mouse. Uninfected K18-hACE2 control mice (n=2) and C57BL/6J wild-type control mice (n=2) were housed in a separate on campus ABSL-1 facility. Aliquots of the inocula and viral stock were saved for back titration using plaque assay for infectious viral titer and RT-qPCR for RNA copy number. All mice were genotyped following Jackson Laboratory protocol # 38170 V2. Mice were assessed daily for signs of disease and changes in weight and temperature. Mice from each group (K18-hACE2, WT) and inoculum dose (10^5 PFU, 10^3 PFU) were euthanized 3 days post infection (dpi) (n=3) and at 6 dpi (n=3). Tissues collected included blood, CNS tissues (olfactory bulb, hippocampus, brainstem, cerebellum, cortex, spinal cord), PNS tissues (autonomic ganglia: superior cervical ganglia-SCG; sensory ganglia: dorsal root ganglia-DRG, trigeminal ganglia-TG), viscera (lung, spleen, liver, kidney, pancreas). Half of the tissues were collected in TRI Reagent for RNA extraction and RT-qPCR and the other half collected in 10% formalin for immunostaining. Brains were split into hemispheres maintaining attachment with the olfactory bulb. One hemisphere was fixed in formalin for immunostaining and the other dissected out into individual brain regions with each placed in TRI Reagent for RT-qPCR. This experiment was repeated as above for reproducibility. Tissue collection from the second experiment was split between TRI Reagent for RT-qPCR as above or flash frozen on dry ice for plaque assay. Blood, spleen, liver, kidney, and pancreas samples from the initial infection study were assessed via RT-qPCR to assess for disseminated infection at 3- and 6- dpi. As these tissues were not the main focus of the investigations, they

were not assessed in the replicate study at 3- and 6- dpi. Lungs from the initial and replicate infection studies were assessed to verify infection at 3- and 6- dpi.

To assess viral spread through nervous tissues at earlier timepoints during infection, and to determine the role, if any that viremia plays verses direct neuronal invasion, K18-hACE2 (n=10) and WT mice (n=10) were infected with 10^5 PFU SARS-CoV-2 as described above and were euthanized 1- and 2-dpi (n=5 of each group/day). Blood, PNS tissues, CNS tissues (with addition of pituitary gland), and salivary glands were collected as described above for RT-qPCR, plaque assays, and immunostaining.

Guinea pig infections. After a two-day acclimation period, three-week-old female Hartley guinea pigs (Hilltop Lab Animals) were infected with either 10^3 PFU (n=12) or 10^5 PFU (n=12) of SARS-CoV-2 as described for K18-hACE2 mice in the ABSL-3 facility (Extended Data Fig 1a.). Uninfected controls (n=2) were housed in the ABSL-2 facility. Guinea pigs were monitored daily as described for mice. Tissue types collected, methods of collection, and downstream assays were the same as described for the mice.

RNA extraction and SARS-CoV-2 specific RT-qPCR. RNA was extracted and RT-qPCR performed as previously described[47]. Briefly, tissues were homogenized in 200 µL TRI Reagent (Fisher Scientific) using a handheld tissue homogenizer with sterile pestles (Cole-Parmer). RNA was extracted using a standard guanidinium thiocyanate-phenol-chloroform extraction. RNA purity and quantity was assessed using a NanoDrop 2000 spectrophotometer (ThermoFisher). SARS-CoV-2 RT-qPCR reactions (10 µL) using the iTaq Universal Probe One-Step Kit (BioRad) and SARS-CoV-2 N1 primers/probe mix (Stock# 10006713; Integrated DNA Technologies) were run on a ViiA 7 Real-Time PCR system (Applied Biosystems) as described in the instructions for use of the CDC 2019-Novel Coronavirus (2019-nCoV) Real-Time RT-PCR assay. Cycle conditions were as follows: Standard setting; 50°C (10 min, 1 cycle), 95°C (2 min, 1 cycle), 95°C then 55°C (30s then 3 s, 45 cycles). Results were reported as genome copy number per 200 ng total RNA.

Immunofluorescence. Tissues were prepared for immunostaining as previously described[48]. Briefly, viscera were fixed in 10% formalin and ganglia were fixed in 4% paraformaldehyde overnight, moved to 30% sucrose overnight, and subsequently embedded in optimal cutting temperature media (ThermoFisher). A Leica CM3050-S cryostat (Leica Biosystems) was used to prepare 7 µm sections from each tissue block. Slides were rinsed in 1X PBS then blocked in 3% normal donkey serum, 0.1% Triton-100X, and 1X PBS for 30 min at room temperature. SARS-CoV-2 N protein was visualized using an Alexa Fluor® 488 conjugated rabbit monoclonal anti-SARS-CoV-2 nucleocapsid antibody at a 1:1000 concentration (NBP2-90988AF488; Novus Biologicals). hACE2 was visualized using an Alexa Fluor® 594 conjugated mouse monoclonal anti-ACE2 antibody at a 1:1000 concentration (sc-390851 AF594; Santa Cruz Biotechnology). NeuN was visualized using an Alexa Fluor® 647 conjugated rabbit monoclonal anti-NeuN antibody at a 1:1000 concentration (ab190565; Abcam). α-d-galactose carbohydrate residues on sensory neurons was visualized using the *Bandeiraea simplicifolia* isolectin B4 (IB4) conjugated to rhodamine at a 1:250 concentration (RL-1102; Vector Laboratories). Tyrosine hydroxylase was visualized using an Alexa Fluor® 594 conjugated mouse monoclonal anti-TH antibody at a 1:500 concentration (818004; Biolegend). Glutamine synthetase was visualized using a mouse monoclonal anti-GS antibody at a 1:100 concentration (MA5-27750; Invitrogen) followed by an Alexa Fluor® 594 conjugated goat anti-mouse monoclonal antibody at a 1:1000 concentration (A11005; Invitrogen). Neuropilin-1 was visualized using a goat polyclonal anti-NRP1 antibody at

a 15 µg/mL concentration (AF566; R&D Systems) followed by an Alexa Fluor® 647 conjugated donkey anti-goat monoclonal antibody at a 1:1000 concentration (ab150135; Abcam). Nuclei were visualized with 4′,6-diamidino-2-phenylindole (DAPI) in SlowFade Diamond antifade mounting medium (ThermoFisher). Primary antibodies were incubated with tissues overnight at 4°C in 1% normal donkey serum, 0.1% Triton-100X, and 1X PBS. Secondary antibodies were incubated with tissues for 1 hour at room temperature.

Confocal microscopy and image analysis. Imaging was performed using a Leica SP8 scanning confocal microscope. Sections of ganglia, brain, and spinal cord were imaged with identical laser power and gain settings within tissue type to account for background immunofluorescence. Cells from in vitro studies were imaged with varying laser power and/or gain due to the wide range of immunofluorescence observed within given experiments. Images were imported into ImageJ and contrast and brightness was adjusted identically across all images within tissue types. 3D models were made using ImageJ and SyGlass VR imaging software.

Plaque assays. Flash frozen tissues were homogenized in Dulbecco's Modified Eagle Medium (DMEM; Fisher Scientific) in bead tubes using a TissueLyser II (Qiagen) for 45 s sessions for three sessions. Ganglia were homogenized in 0.5 mL DMEM due to size. Brain regions and spinal cord segments were homogenized in 1.0 mL of DMEM. The undiluted tissue homogenate as well as a ten-fold dilution of homogenate was inoculated in duplicate onto confluent monolayers of Vero E6 cells in 24-well plates. After 1 h of adsorption, the inoculum was removed, a 0.5% agarose overlay added (DMEM with 8% fetal bovine serum, 1% penicillin/streptomycin, molecular grade agarose), and plates were returned to the incubator for 48 h at 37°C with 5% CO^2. Plates were then fixed with 10% formaldehyde, the agarose overlay removed, and stained with plaque dye. Infectious viral titer is reported as plaque forming units per mL (PFU/mL) of tissue homogenate.

Primary neuronal culture. Neurons from sensory ganglia (TG, DRG) and autonomic ganglia (SCG) were collected from mature mice and cultured as previously described[49-51]. Briefly, ganglia were harvested from 8–10-week-old K18-hACE2 and WT mice and enzymatically digested with a sequential incubation of papain (Worthington) and collagenase/dispase (Sigma-Aldrich) followed by washes in Neurobasal A (Invitrogen) after each digestion. Ganglia were triturated into single cell suspensions via pipette and further washed. SCGs and DRGs were brought to volume in “complete media” containing Neurobasal A with 2% B27 (Invitrogen), 1% penicillin-streptomycin (Thermo Fisher), L-glutamine (Thermo Fisher), fluorodeoxyuridine (Sigma-Aldrich), and neurotrophic factors (PeproTech). Neurons were plated at a concentration of 3,000 neurons/well in Matrigel coated Lab-Tek II 8-well chamber slides or 24-well plates (Thermo Fisher). TGs were collected after separation from debris via density gradient centrifugation using OptiPrep (Sigma-Aldrich) with subsequent washes in Neurobasal A. TGs were plated as described for SCGs and DRGs.

Neuronal infection. Neurons from K18-hACE2 and WT mice were inoculated with SARS-CoV-2 isolate USA-WA1/2020 at 30 MOI in 100 µL Neurobasal A (Invitrogen) for 8-well chamber slides and 200 µL for 24-well plates for 1 h. Following the 1 h adsorption the inoculum was removed, fresh complete media was added (without fluorodeoxyuridine), and neurons were incubated at 37°C with 5% CO2. Aliquots of the inocula and viral stock were saved for back titration using plaque and RT-qPCR.

Quantification of burden of neuronal infection in autonomic and sensory ganglia. To quantify the number of autonomic (SCG) and sensory (DRG) neurons infected per ganglia, 8-well chamber slides were fixed with paraformaldehyde at 1-, 2-, and 3-dpi and stained as described above for the detection of SARS-CoV-2 nucleocapsid. The number of infected neurons from each ganglion were counted for each day, averaged, and reported as the percentage of infected neurons per 500 neurons counted. DRG neurons were chosen as the representative sensory neuron as they had the more dynamic replication kinetics with successive rounds of replication.

Detection of SARS-CoV-2 assembly and release from neurons. To determine if neurons from K18-hACE2 and WT mice are permissive to infection and release of infectious virus, neurons were incubated for up to 5 dpi (depending on availability of neurons from the specific ganglia) with daily sampling. To determine the amount of virus bound to neurons vs that left unbound immediately following incubation with the inoculum, the inoculum and neurons were collected separately and constitute the 0 dpi sample. Daily, media and neurons were collected separately in duplicate (TGs, DRGs) or singularly (SCGs) in 500 µL of LS-TRI Reagent (Fisher Scientific) for RNA extraction and viral genome copy number quantitation via RT-qPCR as described above. Samples were stored at 4°C until processing. For quantification of viral titer in neurons vs that released into the media, neurons and media were collected separately in duplicate (TGs, DRGs) or singularly (SCGs). To correct for evaporation of media throughout the time course the final volume of collected media was brought up 500 µL by adding DMEM prior to plaque assay. Neurons were collected in 500 µL DMEM after scraping with a pipette tip. Samples were immediately stored at -80°C until processing for plaque assay as described above. Following collection of the media but prior to collection of the neurons in TRI reagent or DMEM, the neurons were gently washed with 500 µL DMEM which was then discarded, to remove any residual media containing RNA or virus. A similar rinse was performed immediately after the 1 h inoculation to remove any residual inoculum.

Inhibition of SARS-CoV-2 infection by neuropilin-1 blockade in primary sensory neuronal culture. Primary neuronal cultures of DRGs from K18-hACE2 and WT mice were established as described above. Neurons were pretreated with 100 µM of the NRP-1 antagonist EG00229 (6986; Tocris) dissolved in DMSO prior to infection as described for Caco-2 cells[24]. EG00229 putatively blocks binding between the carboxyl-terminal sequence of SARS-CoV-2 S1 which has a C-end rule (CendR) motif and the extracellular b1b2 CendR binding pocket of NRP-1, which has been suggested as an alternative co-receptor for SARS-CoV-2 in non-neuronal cells [24-26]. Neurons were infected as described above. To determine if NRP-1 blockade impacted SARS-CoV-2 entry and therefore subsequent replication in neurons, neurons and media were collected together in LS-TRI Reagent (Fisher Scientific). RNA was isolated and virus replication assessed via RT-qPCR as described above. Samples were collected at initial peak replication times as determined through our previous neuronal growth kinetics studies (DRG; 3 dpi) to assess if theses peaks were blunted or completely inhibited. Infected neurons from K18-hACE2 and WT mice not treated with EG00229 but with an equivalent amount of DMSO, the solvent for EG00229, served as controls.

Statistics and reproducibility. Sample sizes were not statistically calculated as they are similar to sample sizes used in other SARS-CoV-2 studies using K18-hACE2 mice[14, 15, 18, 20]. Animals were randomly assigned to either inoculum group or control group ensuring the groups were age-matched. Measurements were taken from distinct samples. RT-qPCR and plaque assays were performed in duplicate for each sample when assessing both *in-vivo* and *ex-vivo* infections. RT-

qPCR results that fell below the lower limit for the standard curve (8 copies) after normalization were reported as 0 for inclusion in analysis, no data were excluded. Neuronal infection studies, both immunostaining as well as plaque assay and RT-qPCR studies, were repeated in three separate experiments, with duplicate samples for each ganglion and timepoint in K18-hACE2 and in duplicate in WT mice. Neuropilin-1 inhibition studies were repeated twice, with duplicate samples for each timepoint in K18-hACE2 and WT mice. Mouse infection studies were repeated as described. Guinea pig infection studies were conducted as described. All statistical analyses were performed in JMP Pro 16 (SAS Institute) and confirmed in GraphPad Prism version 8 during figure creation. For statistical analysis, significance was set at $p < 0.05$, calculated as two-tailed. RT-qPCR data was log transformed before analysis to correct for normality of distribution. RT-qPCR data was analyzed using a multifactorial ANOVA. If significance was found, pairwise analysis was performed using Tukey's honestly significant difference (HSD) post hoc test. Inhibitor studies were analyzed using unpaired two-tailed t-tests.

Reporting summary. Further information on research design is available in the Nature Research Reporting Summary linked to this article.

Data availability

Data generated during this study and referenced in this manuscript are available from the corresponding author upon reasonable request.

Methods references

46. Harcourt, J.*, et al.* Severe Acute Respiratory Syndrome Coronavirus 2 from Patient with Coronavirus Disease, United States. *Emerg Infect Dis* **26**, 1266-1273 (2020).
47. Jia, M., Taylor, T.M., Senger, S.M., Ovissipour, R. & Bertke, A.S. SARS-CoV-2 Remains Infectious on Refrigerated Deli Food, Meats, and Fresh Produce for up to 21 Days. *Foods* **11** (2022).
48. Joyce, J.D.*, et al.* Assessment of Two Novel Live-Attenuated Vaccine Candidates for Herpes Simplex Virus 2 (HSV-2) in Guinea Pigs. *Vaccines (Basel)* **9** (2021).
49. Bertke, A.S.*, et al.* A5-positive primary sensory neurons are nonpermissive for productive infection with herpes simplex virus 1 in vitro. *J Virol* **85**, 6669-6677 (2011).
50. Powell-Doherty, R.D., Abbott, A.R.N., Nelson, L.A. & Bertke, A.S. Amyloid-beta and p-Tau Anti-Threat Response to Herpes Simplex Virus 1 Infection in Primary Adult Murine Hippocampal Neurons. *J Virol* **94** (2020).
51. Bertke, A.S.*, et al.* LAT region factors mediating differential neuronal tropism of HSV-1 and HSV-2 do not act in trans. *PLoS One* **7**, e53281 (2012).

Acknowledgments

This research was funded by internal COVID-19 rapid response seed funding from the Fralin Life Sciences Institute at Virginia Tech. The following reagent was deposited by the Centers for Disease Control and Prevention and obtained through BEI Resources, NIAID, NIH: SARS-Related Coronavirus 2, Isolate USA-WA1/2020, NR-52281. Special thanks to Jonathan Auguste, Will Stone, and Addie Hayes for various forms of assistance.

Author contributions

Conceptualization, JDJ, ASB; methodology, JDJ, CKT, ASB; validation, JDJ, CKT, ASB; formal analysis, JDJ, GAM, EH, CKT, ASB; investigation, JDJ, GAM, PG, EH, CKT, ASB; resources, CKT, ASB; data curation, JDJ, CKT, ASB; writing—original draft preparation, JDJ; writing—review and editing, JDJ, CKT, ASB; visualization, JDJ, CKT, ASB; supervision, CKT, ASB; project

816 administration, ASB; funding acquisition, ASB. All authors have read and agreed to the published
817 version of the manuscript.

818 **Competing interests**
819 The authors declare no competing interests.

820

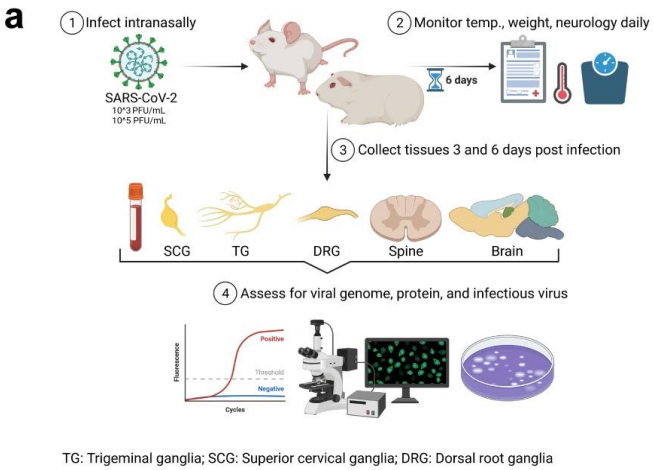

TG: Trigeminal ganglia; SCG: Superior cervical ganglia; DRG: Dorsal root ganglia

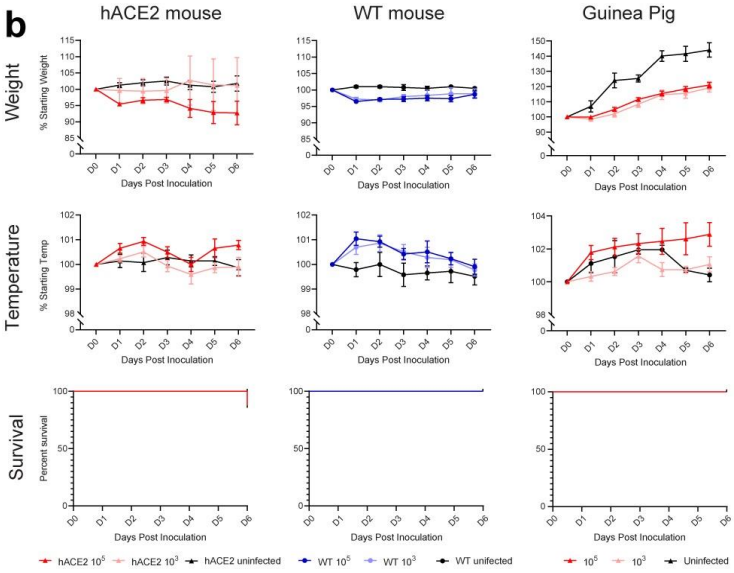

Extended Data Fig 1. | Experimental approach and clinical data for hACE2 mice, WT mice, and guinea pigs. a, Graphical abstract outlining the experimental approach used in both mouse and guinea pig infections highlighting intranasal infection of groups with either 3 log PFU or 5 log PFU SARS-CoV-2, clinical evaluation (temperature, weight, survival), collection of tissues from half of each group at 3- and 6-dpi, and downstream analysis for SARS-CoV-2 RNA copies (RT-qPCR), virus and host antigen (immunostaining), and infectious virus (plaque assay). **b** Clinical data by inoculum group for mice and guinea pigs including weight, temperature, and survival. Weight (grams) for each animal was recorded daily. Weight is reported as the mean percentage increase/decrease for each inoculum group relative to the mean starting weight for that group. The only group to exhibit notable weight loss was the hACE2 mice inoculated with 5 log PFU, which began to lose weight after 3 dpi. Both inoculum groups of guinea pigs gained weight but at a slower rate than uninfected controls. Temperature (°C) for each animal was recorded daily. Temperature is reported as the mean percentage increase/decrease for each inoculum group relative to the mean starting temperature for that group. While transient increases in temperature in the 5 log PFU inoculum groups in both mice and guinea pigs were noted, they were not significant. Kaplan-Meier survival plots were created for each inoculum group. The only group to have mortality was the hACE2 mice inoculated with 5 log PFU. Mortality was noted at 6 dpi (14%, n= 2 of 14).

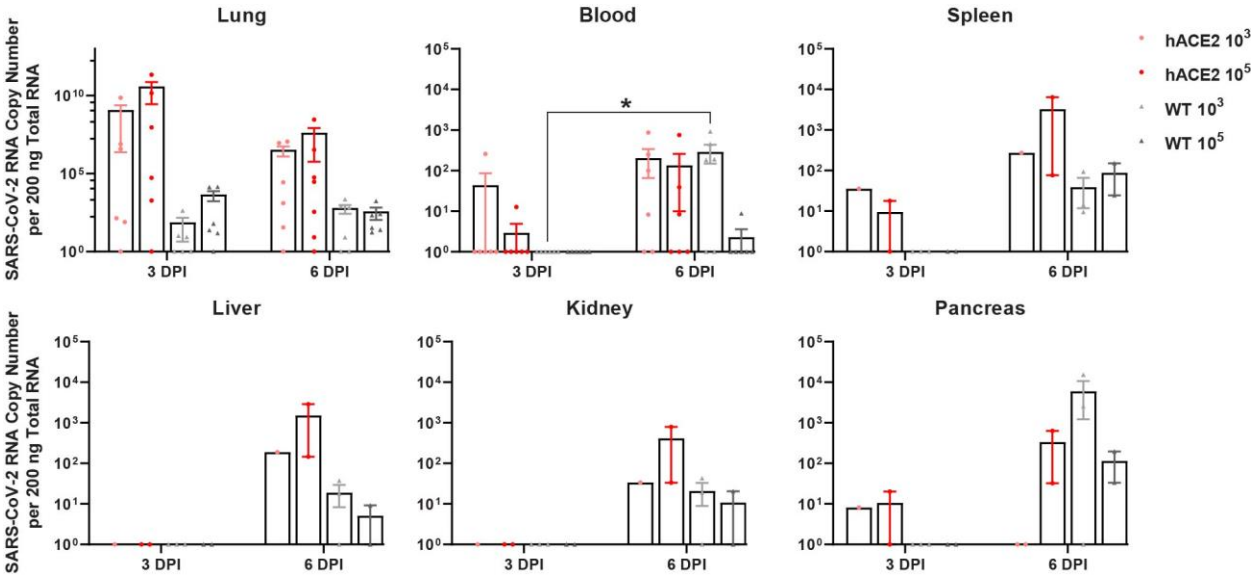

Extended Data Fig 2. | SARS-CoV-2 genome copy numbers in blood and viscera in hACE2 and WT mice. a, SARS-CoV-2 RNA was detected in lungs of hACE2 and WT mice in both inocula groups at both timepoints, which decreased over time. While differences were detected in the lungs ($F(7, 41) = 2.745$, $p = 0.0197$) none were between relevant groups. **b**, Low concentrations of SARS-CoV-2 RNA were detected in the blood of hACE2 in both inoculum groups at 3 dpi and both hACE2 and WT mice in both inoculum groups at 6 dpi. A significant difference ($F(7, 40) = 3.417$, $P = <0.006$) was detected in the WT group inoculated with 10^3 PFU assessed at 3- vs 6-dpi ($p= 0.0321$). Low concentrations of SARS-CoV-2 RNA were also detected in the spleen **c**, liver **d**, kidney **e**, and pancreas **f**, of both inoculum groups in hACE2 and WT mice, mostly appearing at 6 dpi. Data are the mean ± s.e.m. Log transformed RNA genome copy numbers were statistically compared by three-way ANOVA (independent variables: inocula, days post infection, genotype). Pairwise comparisons were conducted using Tukey's HSD post hoc tests. $*p < 0.05$, $**p < 0.01$, $***p < 0.001$.

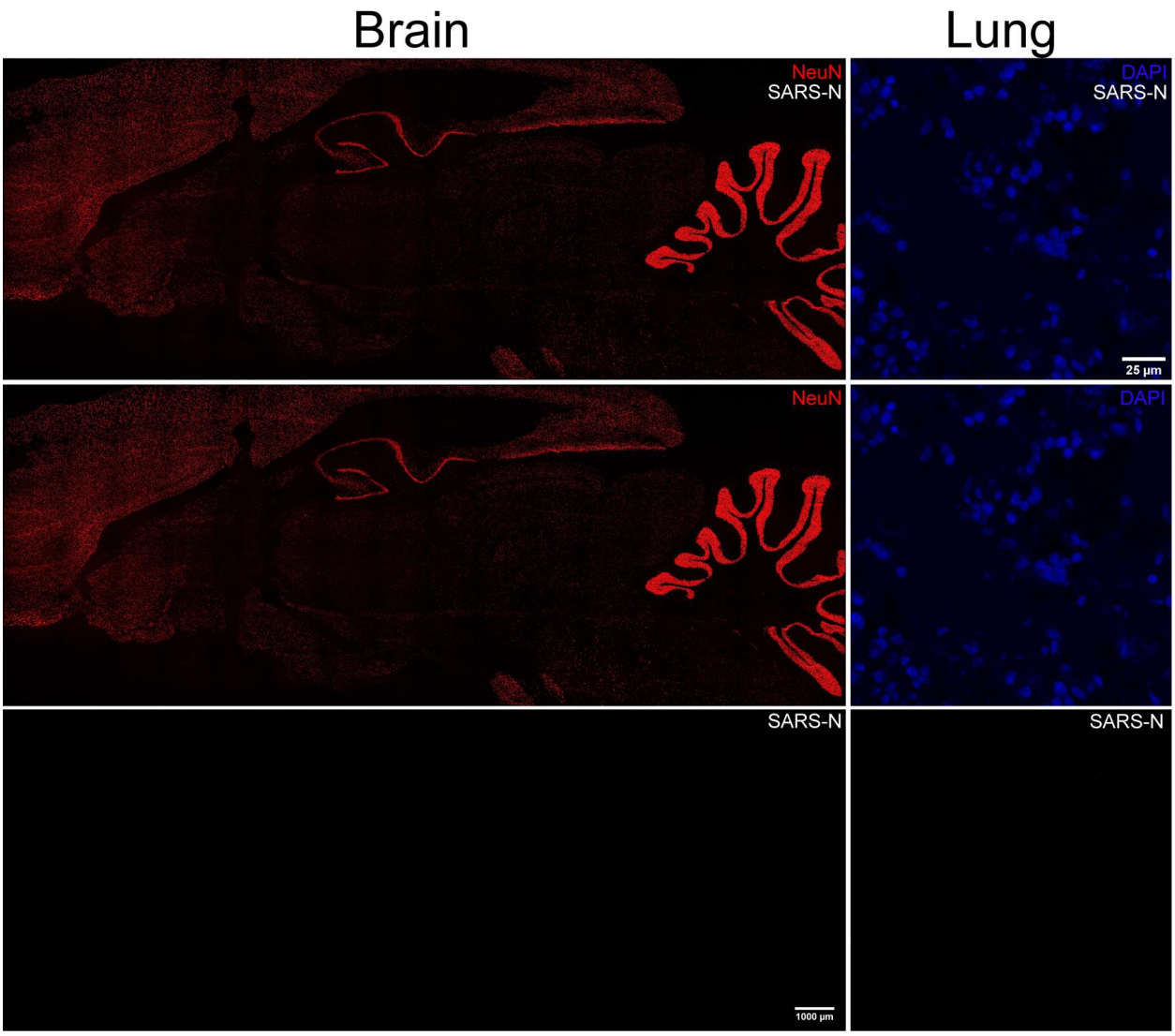

Extended Data Fig 3. | Immunofluorescence for SARS-N protein and NeuN in sections of brain and lung from infected guinea pigs. All images were acquired using a Leica SP8 confocal microscope, using identical image acquisition and ImageJ settings used in Fig 4. No SARS-N was detectable in brains or lungs at 6 dpi.

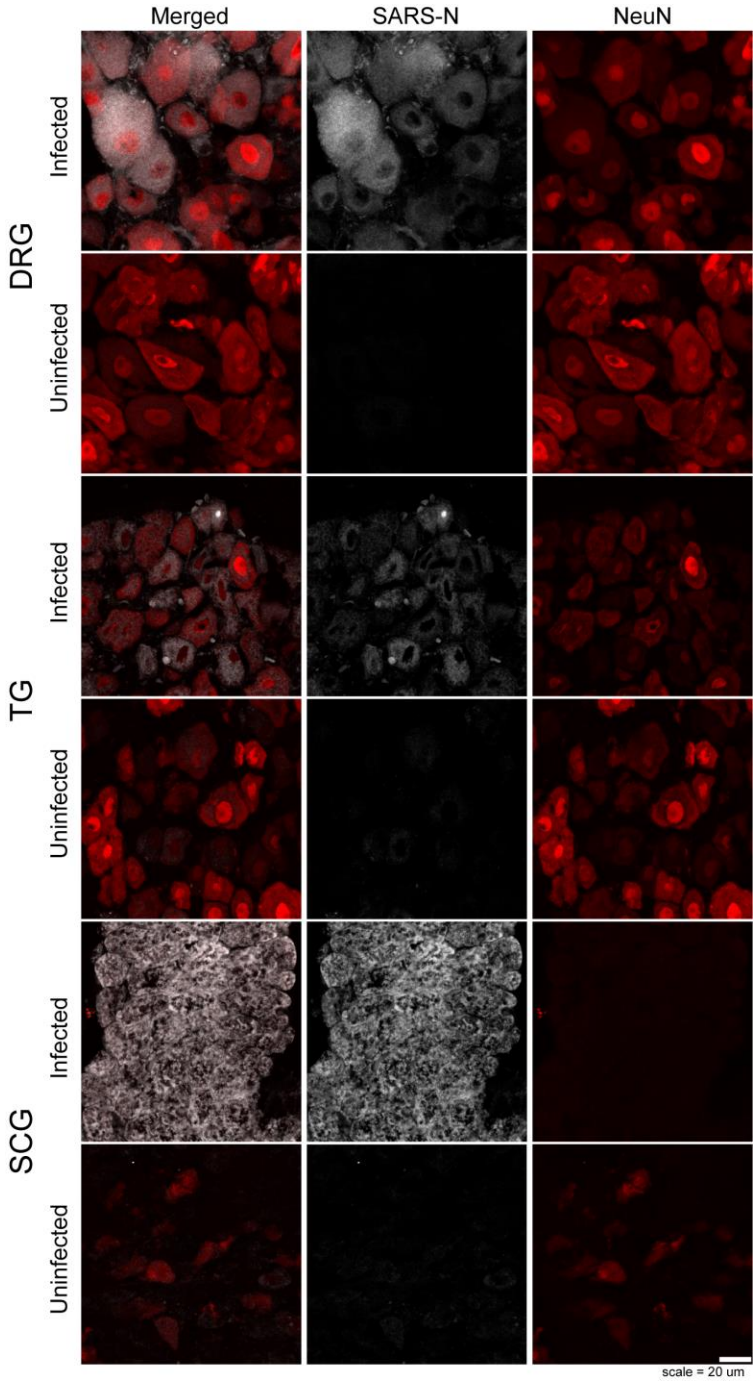

Extended Data Fig 4. | Immunofluorescence for SARS-N protein and NeuN in peripheral ganglia from hACE2 mice. All images were acquired using a Leica SP8 confocal microscope, using identical image acquisition settings (laser power and gain) across all sections shown. All images were colorized, z-projected, and prepared using identical contrast and brightness parameters in ImageJ. SARS-N is present in neurons in the DRG, TG and SCG in infected mice. Minimal background immunofluorescence is observed in sections from uninfected mice. Of note is substantial vacuolization and loss of NeuN immunofluorescence in the infected SCG.

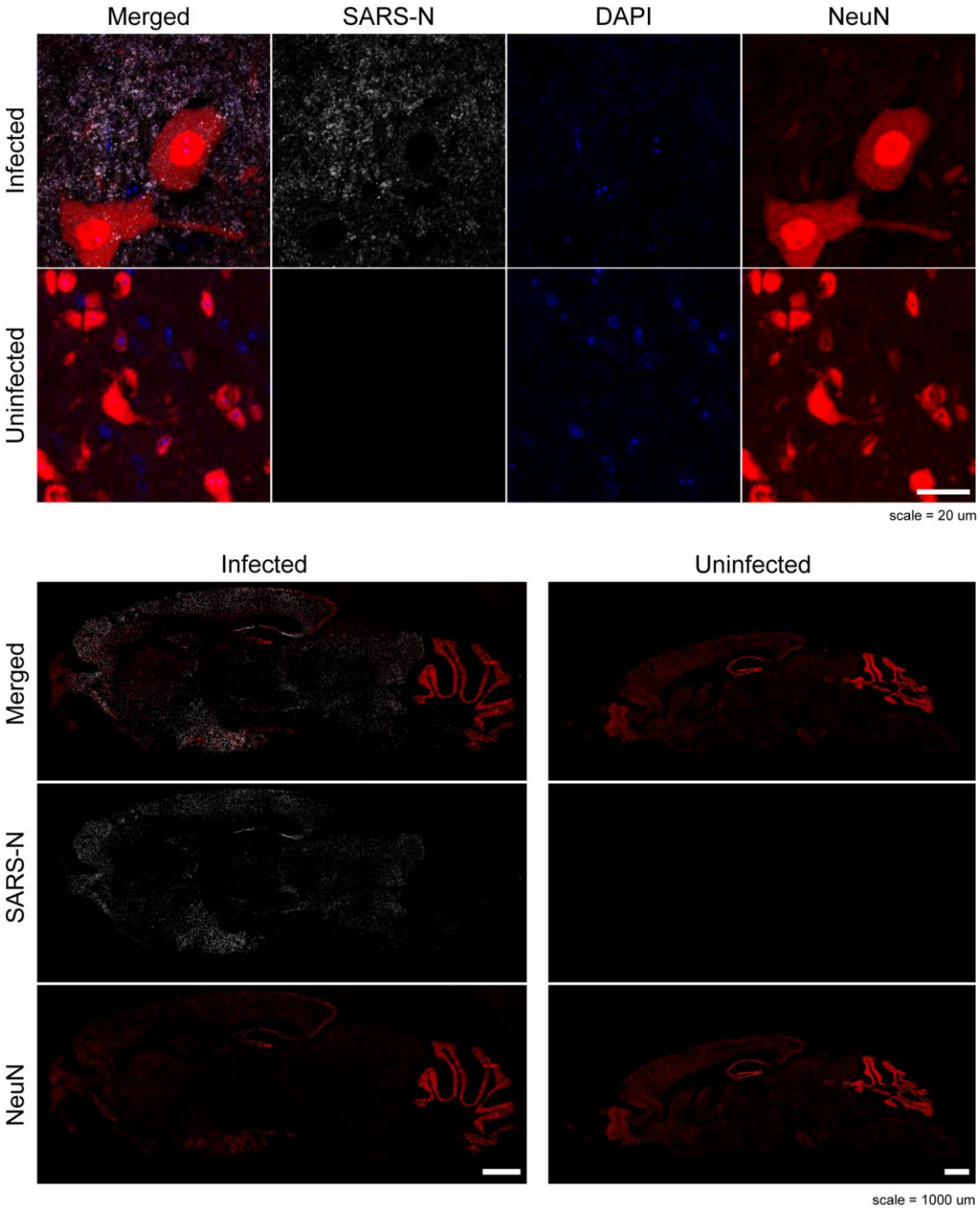

865

866 **Extended Data Fig 5. | Example images of immunofluorescence for SARS-N protein and NeuN in**
867 **sections of spinal cords and brains taken from infected and uninfected hACE2 mice.** All images were
868 acquired using a Leica SP8 confocal microscope, using identical image acquisition settings (laser power
869 and gain) across all sections from each tissue type shown. All images were colorized, z-projected, and
870 prepared using identical contrast and brightness parameters in ImageJ. SARS-N is present in neurons in
871 the spinal cord and brains in infected mice. Minimal background immunofluorescence is observed in
872 sections from uninfected mice. Of note, SARS-N intensity was qualitatively substantially higher in the brain
873 than in the spinal cord.

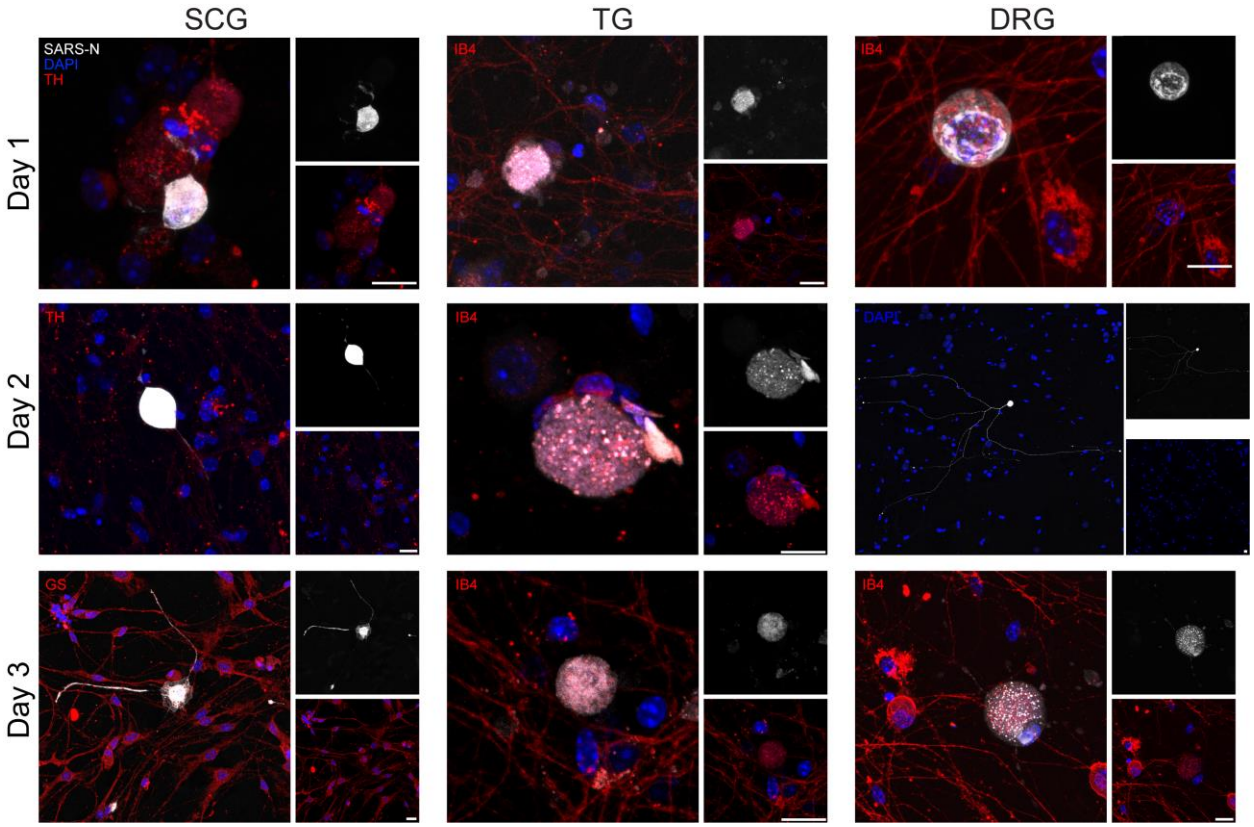

Extended Data Fig 6. | Example images of immunofluorescence for SARS-N protein in *in vitro* cells taken from peripheral ganglia, incubated for two days, then inoculated with SARS-CoV-2. Cells were fixed 1-3 dpi and stained for SARS-N and various counterstains. All images were acquired using a Leica SP8 confocal microscope. Because of substantial variability in intensity of SARS-N immunofluorescence, laser power and gain were adjusted in order to highlight features of each cell. Day 2 DRG is a montage image to show SARS-N detected throughout the neurites of one infected neuron; only DAPI is shown. SARS-N is present in neurons in the SCG, TG, and DRG in infected mice. TH = tyrosine hydroxylase, IB4 = Isolectin-IB4, GS = glutamine synthetase, SARS-N =SARS-CoV-2 nucleocapsid, DAPI = 4′,6-diamidino-2-phenylindole. Scale bar = 20 μm